

Dark Matter Direct Detection with Non-Maxwellian Velocity Structure

Michael Kuhlen^{a,b}, Neal Weiner^c, Jürg Diemand^d, Piero Madau^e, Ben Moore^d, Doug Potter^d, Joachim Stadel^d, Marcel Zemp^f

^a School of Natural Science, Institute for Advanced Study, Princeton, NJ 08540

^b Theoretical Astrophysics Center, University of California Berkeley, Berkeley, CA 94720

^c Center for Cosmology and Particle Physics, Department of Physics, New York University, New York, NY 10003

^d Institute for Theoretical Physics, University of Zurich, 8057 Zurich, Switzerland

^e Department of Astronomy & Astrophysics, University of California Santa Cruz, Santa Cruz, CA 95064

^f Department of Astronomy, University of Michigan, Ann Arbor, Michigan 48109

E-mail: mqk@astro.berkeley.edu, neal.weiner@nyu.edu

ABSTRACT: The velocity distribution function of dark matter particles is expected to show significant departures from a Maxwell-Boltzmann distribution. This can have profound effects on the predicted dark matter - nucleon scattering rates in direct detection experiments, especially for dark matter models in which the scattering is sensitive to the high velocity tail of the distribution, such as inelastic dark matter (iDM) or light (few GeV) dark matter (LDM), and for experiments that require high energy recoil events, such as many directionally sensitive experiments. Here we determine the velocity distribution functions from two of the highest resolution numerical simulations of Galactic dark matter structure (Via Lactea II and GHALO), and study the effects for these scenarios. For directional detection, we find that the observed departures from Maxwell-Boltzmann increase the contrast of the signal and change the typical direction of incoming DM particles. For iDM, the expected signals at direct detection experiments are changed dramatically: the annual modulation can be enhanced by more than a factor two, and the relative rates of DAMA compared to CDMS can change by an order of magnitude, while those compared to CRESST can change by a factor of two. The spectrum of the signal can also change dramatically, with many features arising due to substructure. For LDM the spectral effects are smaller, but changes do arise that improve the compatibility with existing experiments. We find that the phase of the modulation can depend upon energy, which would help discriminate against background should it be found.

KEYWORDS: [dark matter](#), [direct detection](#), [numerical simulations](#).

Contents

1. Introduction	1
2. Results from Numerical Simulations	3
2.1 The Via Lactea and GHALO simulations	3
2.2 Velocity Modulus Distributions	4
2.3 The effects of neglected baryonic physics	7
2.4 Local Escape Speed	7
2.5 Radial and Tangential Distributions	8
2.6 Modulation Amplitude and Peak Day	9
3. Velocity Substructure and Directional Detection	12
4. Implications for DAMA	14
4.1 Inelastic Dark Matter	15
4.1.1 Fitting the DAMA signal	16
4.1.2 Constraining the iDM interpretation of DAMA	16
4.2 Light dark matter	24
5. Discussion	27

1. Introduction

Direct detection experiments aim to detect the low energy nuclear recoil from rare scattering events between dark matter (hereafter DM) particles, assumed to be weakly interacting massive particles (WIMPs), and target nuclei. The event rate and its energy spectrum depend on the properties of the DM distribution at Earth’s location, about 8.5 kpc from the Galactic Center [1]. Typical calculations of the scattering rate assume a “standard halo model” (SHM) consisting of a local DM density of $0.3 \pm 0.1 \text{ GeV cm}^{-3}$ and a Maxwell-Boltzmann (MB) velocity distribution function with a (three-dimensional) dispersion of $270 \pm 70 \text{ km/s}$ [2] truncated at an escape speed of $\sim 550 \text{ km/s}$. Recent numerical simulations of the formation of Galactic-scale DM halos have reached the necessary resolution to directly test these assumptions.

At the same time, absent a positive signal, a set of uniform halo assumptions allows a simple means to compare different experiments. However, in light of the recent results from DAMA/LIBRA [3], confirming earlier results from DAMA/NaI [4], it is important to consider halo model uncertainties when discussing exclusion limits from experiments with different targets, or energy ranges. This is particularly important because proposals such as

light dark matter (LDM) [5, 6] and inelastic dark matter (iDM) [7, 8], which aim to reconcile DAMA with null results from other experiments, sample the high velocity component of the WIMPs preferentially, and it is especially here that the Maxwell-Boltzmann distribution is expected to break down.

In the hierarchical structure formation paradigm of standard cold dark matter cosmology the DM halo of a typical galaxy is built up through the merger of many individual gravitationally bound progenitor halos, which themselves were assembled in a hierarchical fashion. High resolution cosmological simulations, such as Via Lactea [9, 10], GHALO [11], and Aquarius [12], have shown that this merging process is in general incomplete, with the dense cores of many of the merging halos surviving as subhalos orbiting within their respective host halos. During pericenter passages tidal forces can strip off a large fraction of a subhalo’s material, but the resulting cold tidal streams can readily be identified as velocity space substructure. The resulting DM halos are not perfectly phase mixed, and the assumption of a smooth halo is in general not a good one, neither in configuration space nor in velocity space [13].

At 8.5 kpc the Sun is located quite close to the Galactic Center, at least when compared to the overall extent of the Milky Way’s DM halo ($r_{\text{vir}} \sim 200 - 300$ kpc). This central region is notoriously difficult for cosmological numerical simulations to resolve, as very high particle numbers and very short time steps are required to avoid the so-called “overmerging problem” [14], which has until recently resulted in an artificially smooth central halo devoid of any substructure. With the advent of $\mathcal{O}(10^9)$ particle simulations at the Galactic scale this problem finally seems to have been overcome, with hundreds of subhalos identified at $\lesssim 20$ kpc. Nevertheless the local phase space structure is far from completely resolved, and likely never will be through direct numerical simulation. Any estimation of the importance of local density or velocity substructure based on cosmological simulation must thus rely on extrapolations over many orders of magnitude below its resolution limit.

Local density variations due to the clumpiness of the DM halo are unlikely to significantly affect the direct detection scattering rate. Based on the Aquarius Project suite of numerical simulations, Vogelsberger et al. (2008) [15] report that at more than 99.9% confidence the DM density at the Sun’s location differs by less than 15% from the average over a constant density ellipsoidal shell. Extrapolating from their numerical convergence study they estimate a probability of 10^{-4} of the Sun residing in a bound subhalo of any mass. Analytical work by Kamionkowski & Koushiappas (2008) [16] predicts a positively skewed density distribution with local densities as low as one tenth the mean value, but probably not much less than half.

The situation for velocity substructure is less clear. It is well established that numerically simulated dark matter halos exhibit significant velocity anisotropy and global departures from a Maxwell-Boltzmann distribution [17, 18, 19, 20]. The implications for direct detection experiments of these global departures from the standard Maxwellian model have previously been investigated in the context of a standard WIMP model [21, 22, 23, 24] and for inelastic dark matter [25, 26], and they were found to result in appreciable differences (factor of a few) in the total event rates and the annual modulation signal. Most recently Vogelsberger et al. (2008) reported significant structure (“wiggles”) in the ve-

locity distribution function measured in their high-resolution Aquarius simulations, which they attributed to events in the halo’s mass assembly history. Their analysis concluded that velocity substructure due to bound subhalos or unbound tidal streams, however, does not influence the detector signals, since it makes up a highly sub-dominant mass fraction locally.

The aim of this paper is take a closer look at this velocity space substructure and to examine its impact on the direct detection signal for models that are particularly sensitive to the high velocity tail, such as LDM or iDM. In contrast to Vogelsberger et al. (2008), we find that both global and local departures from the best-fit Maxwell-Boltzmann distribution can significantly affect the total event rate, the annual modulation, and the recoil energy spectrum. Parameter exclusion limits derived using a standard MB halo model are likely to be overly restrictive.

This paper is organized as follows: in Section 2 we present velocity distribution functions derived from the high-resolution numerical simulations Via Lactea II and GHALO. In Section 3 we look at the implications of high velocity substructure for direct detection experiments with directional sensitivity. In Section 4 we consider iDM and LDM models and show how the observed local and global departures from the MB model affect scattering event rates and recoil spectra at several ongoing direct detection experiments, and how this modifies parameter exclusion limits. A summary and discussion of our results can be found in Section 5.

2. Results from Numerical Simulations

The nuclear scattering event rate depends on the size of the detector, the type of target material, the scattering cross section, and the number density and velocity distribution of the impinging DM particles. We defer calculations of the expected event rate for various experimental setups and types of DM models to section 4, and focus in this section on the particle velocity distributions, which we determine directly from numerical simulations.

2.1 The Via Lactea and GHALO simulations

Our analysis is based on two of the currently highest resolution numerical simulations of Galactic DM structure: Via Lactea II (VL2) [10] and GHALO [11]. Both are cosmological cold DM N-body simulations that follow the hierarchical growth and evolution of a Milky-Way-scale halo and its substructure from initial conditions in the linear regime ($z = 104$ for VL2, $z = 58$ for GHALO) down to the present epoch. For details about the setup of the simulations we refer the reader to the above references. The VL2 host halo is resolved with ~ 400 million particles of mass $m_p = 4,100 M_\odot$ within its virial radius¹ of $r_{\text{vir}} = 309$ kpc and has a mass of $M_{\text{halo}} = 1.7 \times 10^{12} M_\odot$ and peak circular velocity $V_{\text{max}} = 201.3$ km/s. The GHALO host is somewhat less massive, $M_{\text{halo}} = 1.1 \times 10^{12} M_\odot$ and $V_{\text{max}} = 152.7$ km/s, but even more highly resolved, with 1.1 billion particles of mass $m_p = 1,000 M_\odot$ within its $r_{\text{vir}} = 267$ kpc. For reference we show the circular velocity of the two halos in

¹ r_{vir} is defined as the radius enclosing a density of $\Delta_{\text{vir}} = 389$ times the background density.

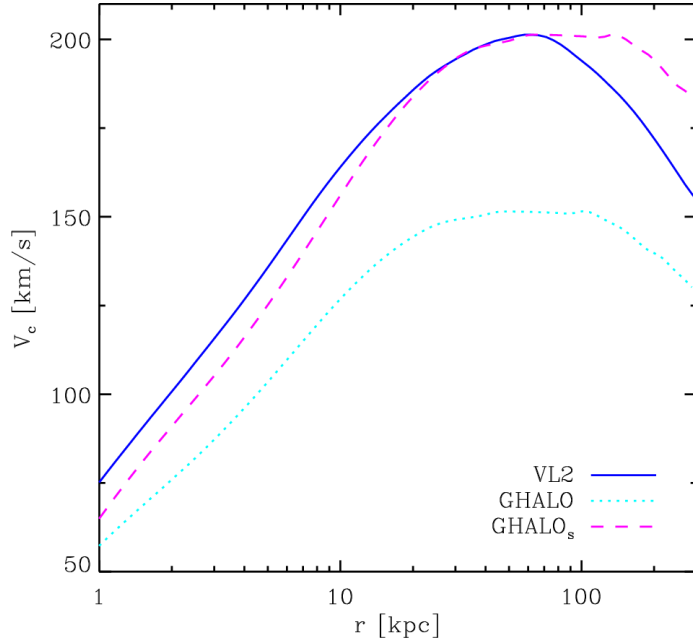


Figure 1: Circular velocity profiles of the VL2, GHALO, and GHALO_s host halos.

Fig.1. In order to facilitate a more direct comparison between the two halos, we have also scaled GHALO to match VL2’s V_{\max} by multiplying the simulation’s length and velocity units by a factor $f = V_{\max}(\text{VL2})/V_{\max}(\text{GHALO}) = 1.32$, and the mass unit by f^3 . We refer to this model as GHALO_s. The circular velocity of these three halos at 8.5 kpc is 158.1, 121.7, and 148.9 km/s for VL2, GHALO, and GHALO_s, respectively.

2.2 Velocity Modulus Distributions

The DM-nucleon scattering event rate is directly proportional to

$$g(v_{\min}) = \int_{v_{\min}}^{\infty} \frac{f(v)}{v} dv, \quad (2.1)$$

where $f(v)$ is the DM velocity distribution function in the Earth’s rest frame and $v_{\min}(E_R)$ is the minimum velocity that can result in a scattering with a given nuclear recoil energy E_R . For a target with nuclear mass m_N and a WIMP/nucleon reduced mass $\mu = m_N m_\chi / (m_N + m_\chi)$, $v_{\min}(E_R)$ is given by

$$\left(\frac{v_{\min}}{c}\right)^2 = \frac{1}{2} \frac{m_N E_R}{\mu^2} \left(1 + \frac{\mu}{m_N E_R} \delta\right)^2. \quad (2.2)$$

The δ refers to the possible mass splitting between the incoming and outgoing DM particle, which would be 0 for standard and light DM and $\mathcal{O}(100 \text{ keV})$ for inelastic DM.

We determine $f(v)$ in the halo rest frame directly from the particle velocities in our numerical simulations, and in the Earth’s rest frame by first applying a Galilean velocity boost by $v_{\oplus}(t)$. The Earth’s velocity with respect to the Galactic center is the sum of the

local standard of rest (LSR) circular velocity around the Galactic center, the Sun’s peculiar motion with respect to the LSR, and the Earth’s orbital velocity with respect to the Sun,

$$\vec{v}_{\oplus}(t) = \vec{v}_{\text{LSR}} + \vec{v}_{\text{pec}} + \vec{v}_{\text{orbit}}(t). \quad (2.3)$$

We follow the prescription given in Chang et al. (2008) [27] and set $\vec{v}_{\text{LSR}} = (0, 220, 0)$ km/s, $\vec{v}_{\text{pec}} = (10.00, 5.23, 7.17)$ km/s [28], and $\vec{v}_{\text{orbit}}(t)$ as specified in reference [29]. The velocities are given in the conventional (U, V, W) coordinate system where U refers to motion radially inwards towards the Galactic center, V in the direction of Galactic rotation, and W vertically upwards out of the plane of the disk. We associate these three velocity coordinates with the (v_r, v_θ, v_ϕ) coordinates of the simulation particles.

The Earth’s orbital motion around the Sun results in the well-known annual modulation of the scattering rate, which the DAMA collaboration claims to have detected at very high statistical significance [3]. For the SHM the peak of this modulation occurs around June 2nd, when the Earth’s relative motion with respect to the Galactic DM halo is maximized.

We have measured the DM velocity distribution from all particles in a 1 kpc wide spherical shell ($8 \text{ kpc} < r < 9 \text{ kpc}$), containing 2.1, 5.4, and 3.6 million particles in VL2, GHALO, and GHALO_s, respectively. The large particle numbers in these measurements result in a very small statistical uncertainty, but fail to capture any local variations. To address this we have also determined $f(v)$ from the particles in 100 randomly distributed sample spheres centered at 8.5 kpc. These sample spheres have radii of 1.5 kpc for VL2 and 1 kpc for GHALO and GHALO_s, and contain a median of 31,281, 21,740, and 14,437 particles in the three simulations.²

The resulting distributions, both in the halo rest frame and translated into Earth’s rest frame, are shown in Fig. 2. The shell averaged distribution is plotted with a solid line, while the light and dark green shaded regions indicate the 68% scatter around the median and the absolute minimum and maximum values of the distribution over the 100 sample spheres. For comparison we have also overplotted the best-fitting Maxwell-Boltzmann (hereafter MB) distributions, with 1D velocity dispersion of $\sigma_{1\text{D}} = 130, 100, \text{ and } 130$ km/s. These clearly underpredict both the low and high velocity tails of the actual distribution. This is not a new result and has previously been found in cosmological numerical simulations [17, 18, 19, 15]. Actually there is no reason to assume that a self-gravitating, dissipationless system would have a locally Maxwellian velocity distribution, and in fact it has been shown that self-consistent, stable models of cuspy DM structures require just such non-Gaussianity [30, 31].

In addition to its overall non-Maxwellian nature, we notice several broad bumps present in both the shell averaged and, at very similar speeds, in the sub-sample $f(v)$. Similar features were reported by Vogelsberger et al. (2008) [15] for the host halos of their completely independent Aquarius simulations, and thus appear to be robust predictions of hierarchically formed collisionless objects. Vogelsberger et al. also showed that the broad bumps

²Tables of $g(v_{\text{min}})$ determined from the spherical shell and the 100 sample spheres, and tracing the annual modulation over 12 evenly spaced output times, are available for download at <http://astro.berkeley.edu/~mqk/dmdd/>.

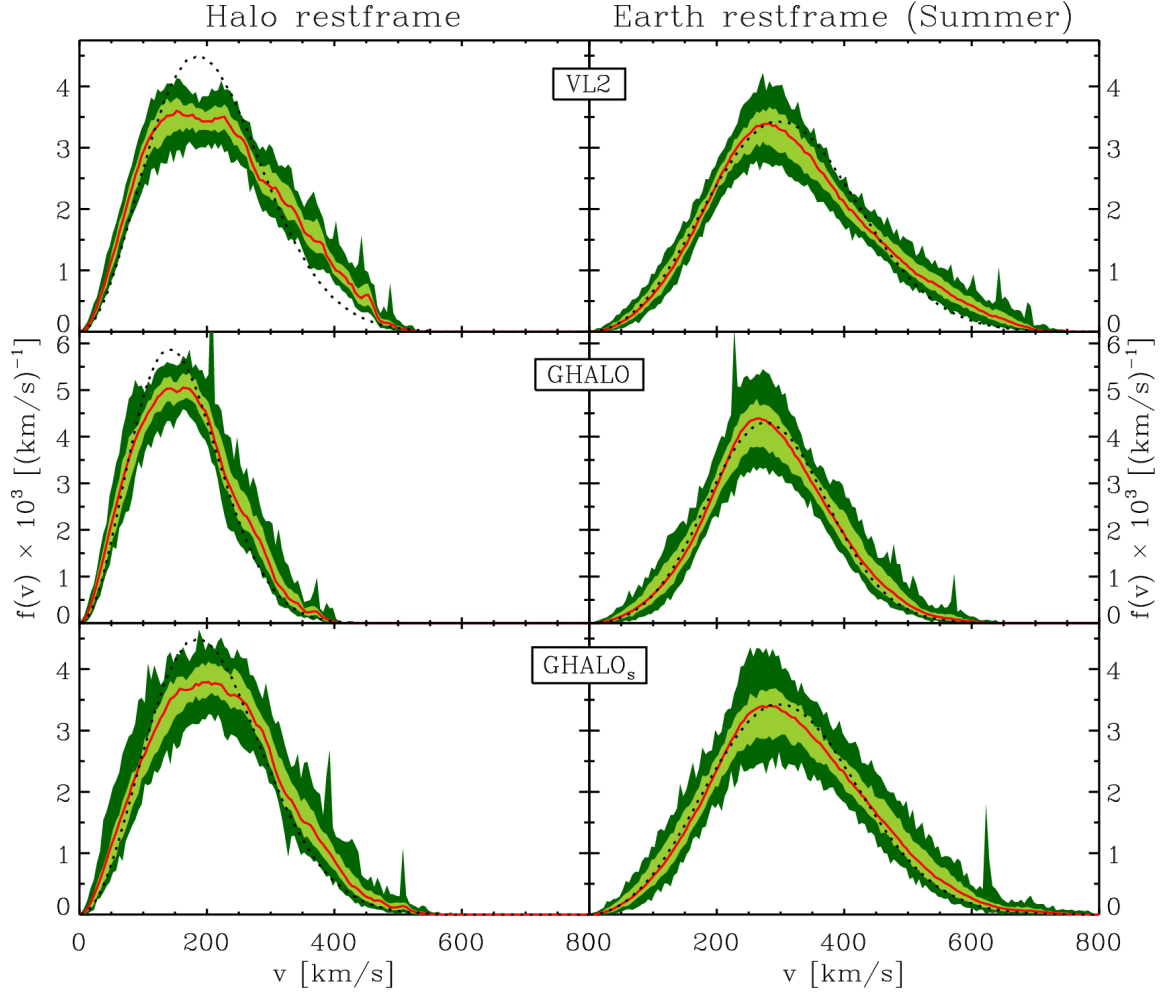


Figure 2: Velocity distribution functions: the left panels are in the host halo’s restframe, the right panels in the restframe of the Earth on June 2nd, the peak of the Earth’s velocity relative to Galactic DM halo. The solid red line is the distribution for all particles in a 1 kpc wide shell centered at 8.5 kpc, the light and dark green shaded regions denote the 68% scatter around the median and the minimum and maximum values over the 100 sample spheres, and the dotted line represents the best-fitting Maxwell-Boltzmann distribution.

are independent of location and persistent in time and hence reflect the detailed assembly history of the host halo, rather than individual streams or subhalos. The extrema of the sub-sample distributions, however, exhibit numerous distinctive narrow spikes at certain velocities, and these are due to just such discrete structures. Note that although only a small fraction of sample spheres exhibits such spikes, they are clearly present in some spheres in all three simulations. The Galilean transform into the Earth’s rest frame washes out most of the broad bumps, but the spikes remain visible, especially in the high velocity tails, where they can profoundly affect the scattering rates for inelastic and light DM models (see Section 4).

In order to assess the dependence of these features on the sample sphere size, we also considered for the VL2 simulation sphere radii of 1 and 2 kpc, containing a median of 9,200 and 74,398 particles, respectively. The coarse features of the distributions persist, but of course the prevalence of the spikes increases with sample sphere size, as more of the substructure is probed. It is difficult to assess with our simulations the true likelihood of significant local velocity substructure, as it depends on the abundance and physical extent of subhalos and tidal streams many orders of magnitude below the length scales that we can accurately resolve. Higher resolution numerical simulations, as well as analytical models [32], perhaps in conjunction with simulations [33], will be necessary to settle this question.

2.3 The effects of neglected baryonic physics

The values of σ_{1D} we report here may appear surprisingly low to a reader familiar with the standard isothermal MB halo assumption of $\langle v^2 \rangle = 3\sigma_{1D}^2 = 3/2 v_0^2$, where v_0 , the peak of the MB distribution, i.e. the most probable speed, is assumed to be equal to the rotation velocity of the Sun around the galaxy, $v_0 \simeq 220$ km/s. In this standard model σ_{1D} would be 156 km/s, considerably higher than our values of 130 km/s and 100 km/s, respectively. In fact, the local circular velocity v_c and velocity dispersion σ are only indirectly related and not necessarily equal. While v_c is set by the local radial gradient of the potential, σ depends on the shape of the potential at exterior radii. For a non-rotating spherical system the relation between $v_c(r)$ and the radial velocity dispersion $\sigma_r(r)$ is given by

$$v_c^2 = -\sigma_r^2 \left(\frac{d \ln \rho}{d \ln r} + \frac{d \ln \sigma_r^2}{d \ln r} + 2\beta \right), \quad (2.4)$$

where $\frac{d \ln \rho}{d \ln r} \equiv \gamma(r)$ is the logarithmic slope of the density profile and $\beta(r) \equiv 1 - \sigma_\theta^2/\sigma_r^2$ is the velocity anisotropy. In a singular isothermal sphere ($\gamma = -2$, $\frac{d \ln \sigma_r^2}{d \ln r} = 0$, $\beta = 0$) we have $v_c = v_0$, but for an NFW profile $v_c/v_0 \approx 0.88$ at $r = r_s/2$. In the VL2 and GHALO host halos the relation is $v_c/v_0 = 0.85$ and 0.86 , respectively.

A central baryonic condensation in the form of a Galactic disk and bulge will deepen the central potential, raise the local circular velocity to ~ 220 km/s, and increase the velocity dispersion of DM particles at the Sun's location. Since the VL2 and GHALO simulations do not include baryonic physics, it is not surprising that the values of v_c and v_0 at 8.5 kpc are lower than appropriate for our Milky Way galaxy. The main focus of our work here is to investigate the effects of global and local variations from the MB assumption, and therefore we compare our results to the best-fitting MB model ($v_0 = 184$ km/s for VL2 and GHALO_s and 141 km/s for GHALO) instead of the standard MB halo model ($v_0 = 220$ km/s). In principle we could have scaled just the velocities up to give $v_0 = 220$ km/s, but this would remove many of the effects of substructure by pushing it above the escape velocity. Thus, we use VL2 and GHALO_s simulations for the parameter exclusions plots in Section 4, but it should be recognized, that the velocity dispersion is somewhat lower than in conventional MB halo parameterizations.

2.4 Local Escape Speed

The escape speed from the Sun's location in the Galactic halo is another factor that can

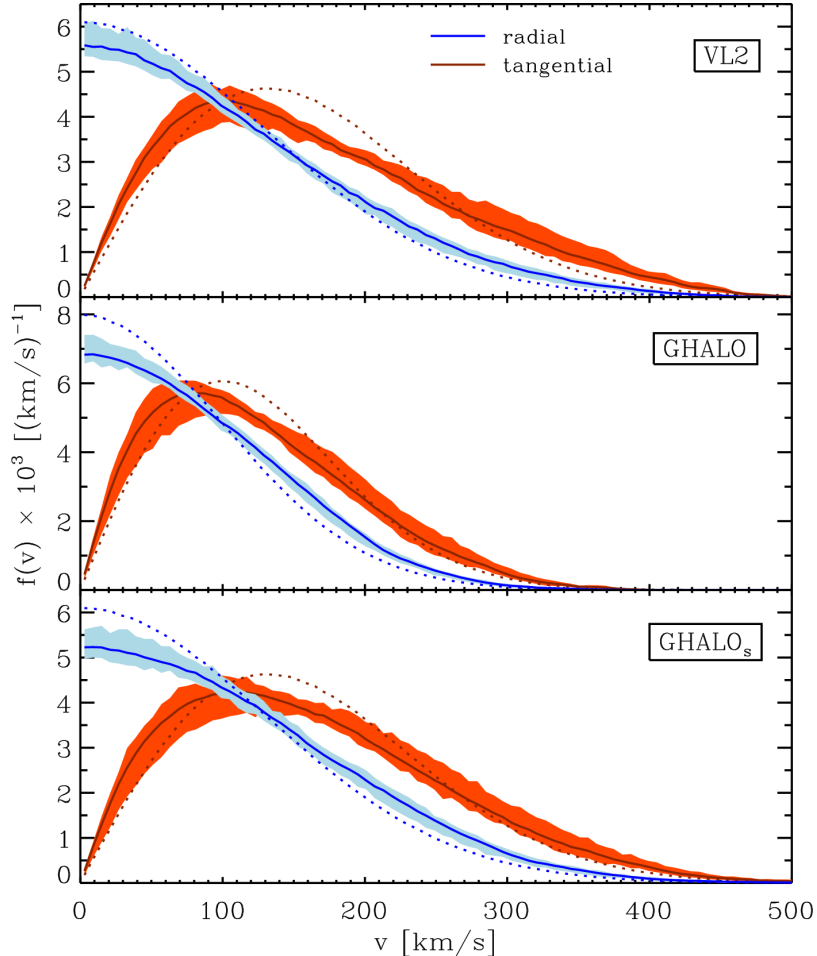


Figure 3: Radial and tangential velocity distribution functions. The solid lines show the shell average, the shaded range the 68% scatter around the median, and the dotted curve shows the best-fit MB model.

strongly affect scattering rates, especially for inelastic and light DM models. The RAVE survey’s sample of high-velocity stars constrains the Galactic escape velocity to lie between 498 and 608 km/s at 90% confidence, with a median likelihood of 544 km/s [34]. This is in good agreement with the highest halo rest frame speed of any particle in our 8.5 kpc spherical shells, namely 550 km/s in VL2 and 586 km/s in GHALO_s. The lower V_{max} of the GHALO host is reflected in a significantly lower escape speed, only 433 km/s. The corresponding maximum speeds in the Earth rest frame are 735-761, 773-802, and 634-660 km/s, where the range refers to the modulation introduced by the Earth’s orbit around the Sun.

2.5 Radial and Tangential Distributions

For comparison with past work [25, 24] we also present separately the distribution functions of the radial v_r and tangential $v_t = \sqrt{v_\theta^2 + v_\phi^2}$ velocity components in Fig. 3. We fit these distributions with functions like the ones in Fairbairn & Schwetz (2009) [24], except that

we don't normalize the velocities by the square root of the gravitational potential at the particles' location and instead provide separate fits for each simulation. We also include an estimate of the variance due to local velocity substructure by separately fitting the distribution in each of the sample spheres. The fitting functions are

$$f(v_r) = \frac{1}{N_r} \exp \left[- \left(\frac{v_r^2}{\bar{v}_r^2} \right)^{\alpha_r} \right] \quad (2.5)$$

$$f(v_t) = \frac{v_t}{N_t} \exp \left[- \left(\frac{v_t^2}{\bar{v}_t^2} \right)^{\alpha_t} \right], \quad (2.6)$$

and the parameters of these fits are listed in Table 2.5. The normalizations N_r and N_t can readily be obtained numerically for a given set of parameters by ensuring that the distributions integrate to unity.

		radial				tangential			
		shell	median	16 th	84 th	shell	median	16 th	84 th
VL2	$\bar{v}_{r,t}$ [km/s]	202.4	199.9	185.5	212.7	128.9	135.1	124.2	148.9
	$\alpha_{r,t}$	0.934	0.941	0.877	0.985	0.642	0.657	0.638	0.674
GHALO	$\bar{v}_{r,t}$ [km/s]	167.9	163.6	156.4	173.0	103.1	114.3	93.21	137.0
	$\alpha_{r,t}$	1.12	1.11	1.02	1.20	0.685	0.719	0.666	0.819
GHALO _s	$\bar{v}_{r,t}$ [km/s]	217.9	213.8	202.3	226.6	138.2	162.2	125.1	183.1
	$\alpha_{r,t}$	1.11	1.11	1.01	1.18	0.687	0.759	0.664	0.842

Table 1: Radial and tangential velocity distribution fit parameters (see Eqs. 2.5 and 2.6). The columns labeled “shell” refer to the fit for all particles in the 1 kpc wide shell centered on 8.5 kpc, whereas the following three columns give the median as well as the 16th and 84th percentile of the distribution of fits over the 100 sample spheres (see text for more detail).

2.6 Modulation Amplitude and Peak Day

The annual modulation of the scattering rate $g(v_{\min})$ (Eq. 2.1) grows with v_{\min} , since a reduction in the number of particles able to scatter makes the summer-to-winter difference relatively more important. At sufficiently high velocities the modulation amplitude can even reach unity, when during the winter there simply aren't any particles with velocities above v_{\min} .

The expected modulation amplitude for a given experiment is then determined by the relation between the measured recoil energy E_R and v_{\min} , see Eq. 2.2. There are important qualitative difference between standard DM models ($\delta = 0$) and inelastic models ($\delta \sim 100$ keV). Inelastic DM models require a higher v_{\min} for a given E_R , resulting in a lower total scattering rate and a more pronounced modulation. Furthermore, while for standard DM v_{\min} grows with E_R , in inelastic models v_{\min} typically falls with E_R (for $\delta > E_R m_N / \mu$).

In the left panels of Fig. 4 we show the v_{\min} dependence of the annual modulation amplitude, $(\max(g(v_{\min})) - \min) / (\max + \min)$ as measured in our simulations. We focus on the high v_{\min} region that is relevant for inelastic and light dark matter models, as well as directional detection experiments. In VL2 and GHALO_s the shell averaged modulation

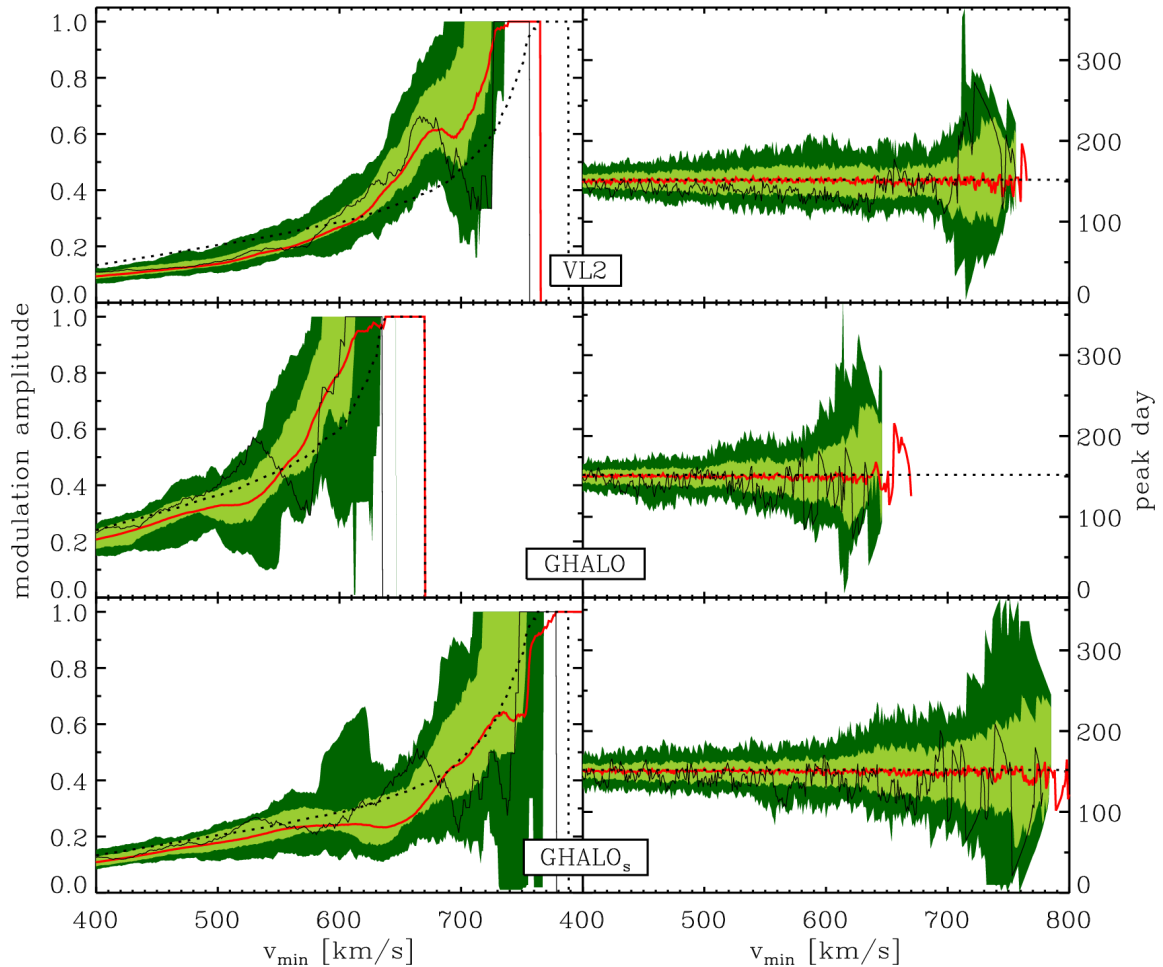


Figure 4: The amplitude (left panels) and peak day (right) as a function of v_{\min} . The solid red line indicates the shell averaged quantities, and the dotted line the best-fit MB distribution. The light and green shaded regions cover the central 68% region around the median and the minimum and maximum values of the distribution over the 100 sample spheres. The thin black line shows the behaviour of one example sample sphere.

amplitude (solid red line) rises from about 20% at $v_{\min} = 400$ km/s to unity at ~ 750 km/s. The GHALO amplitudes are shifted to lower v_{\min} , growing from 40% at 400 km/s to 100% already at ~ 600 km/s. The strong high velocity tails of $f(v)$ (Fig. 2) result in somewhat lower modulation amplitudes compared to the best-fit MB distributions (dotted line). At the very highest velocities $f(v)$ drops below the Maxwellian distribution in VL2 and GHALO, and this leads to the rise in amplitudes above the Maxwellian case for $v_{\min} > 600$ and 550 km/s, respectively. In GHALO_s the distribution more closely follows the MB fit, and only barely rises above it at $v_{\min} > 670$ km/s. Interestingly, all three simulations exhibit a pronounced dip in the modulation amplitude at close to the highest v_{\min} . These correspond to bumps in $f(v)$ discussed in Section 2.2.

As before, the light and dark shaded green regions in Fig. 4 cover the 68% region

around the median and the extrema of the distribution over the 100 sample spheres. Over most of the range of v_{\min} , the typical modulation amplitude in a sample sphere differs from the spherical shell average by less than 10%. The extrema of the distribution, however, can differ much more significantly, especially at higher velocities. If the Sun happens to be passing through a fast moving subhalo or tidal stream, the typical velocity of impinging DM particles can greatly differ from the smooth halo expectation, leading to an increase (or decrease) in the overall scattering rate and modulation amplitude. For a conventional massive (> 10 GeV) DM particle, scattering events are dominated by the peak of the velocity distribution function and the effects from streams or subhalos are washed out and typically negligible [15]. However, whenever scattering events are dominated by particles on the high velocity tail of the distribution, either because of a velocity threshold (inelastic DM), a particularly low particle mass (light DM), or for detectors intrinsically sensitive to only high recoil energies (e.g. many directionally sensitive detectors), the presence of velocity substructure can have a profound impact on the event rates.

Another potentially interesting signature of velocity space structure is the shift in the peak day of the annual modulation, as was explored in [22]. For an isotropic velocity distribution (e.g. MB) the peak day is independent of v_{\min} and occurs around the beginning of June. Any kind of departure from isotropy, however, would leave its signature as a change in the phase of the modulation. In the most extreme case of a very massive DM stream moving in exactly the same direction as the Sun, the phase of modulation could flip completely, with the maximum scattering amplitude occurring in the winter.

In the right panel of Fig. 4 we show the v_{\min} dependence of the peak day as measured in our simulations. The spherical shell average is consistent with a phase shift of zero, except at the very highest velocities where a few discrete velocity structures dominate the shell average and introduce small velocity dependent phase shifts. The peak days in the sample spheres, however, often differ by ~ 20 days from the fiducial value. As an example we have plotted a curve for one of the sample spheres. The peak day determination appears to be quite noisy here, but since the particle numbers are still fairly large ($N(> v_{\min}) = 9114, 802, 105$ for $v_{\min} = 400, 600, 670$ km/s in the VL2 sample sphere shown), we believe that the variations in peak day arise from actual velocity structure rather than discreteness noise. The 68% scatter of the phase shifts over the 100 sample spheres remains remarkable constant at $\pm 10 - 20$ days throughout most of the v_{\min} range. At higher velocities ($v_{\min} > 600 - 700$ km/s) the typical phase shifts grow to ~ 50 days, which could be due to the increasing relative importance of individual streams, but may also be due to particle discreteness noise. *Based on our measurements we would expect some amount of variation in the peak day as a function recoil energy. As it is hard to imagine any background contamination to exhibit such a phase shift, this raises the possibility of such a measurement confirming a DM origin of the DAMA modulation signal.*

We conclude this section by noting that our simulations reveal both global (shell averaged) and local (sample spheres) departures from the standard halo model in velocity space. These can have a significant effects on the overall scattering rate, as well as on the amplitude and peak day of the annual modulation thereof. In the next section we go on to explore how these effects translate into predicted detection rates for actual direct

detection experiments, and how they modify parameter exclusions plots based on existing null-detections.

3. Velocity Substructure and Directional Detection

Up to this point we have focused on the integrated features of the halo, i.e., $f(v)$ or $g(v_{\min})$, but there are many more structures that appear that are not pronounced in these measures. In particular, the presence of clumps and streams, while contributing to the bumps and wiggles of these functions, can be more pronounced when the direction of the particles’ motions, rather than just the amplitude, is considered. These features are especially important for directional WIMP detectors, such as DRIFT [35], NEWAGE [36] and DMTPC [37], where the presence of such structures could show up as a dramatic signal. Although we do not discuss it here, such directional experiments have been argued to be especially important for testing inelastic models [38, 39].

To quantify this, we begin by searching for “hotspots” on the sky. To do this, we make a map of the sky in HealPix, and consider the flux of WIMPs from each direction in the sky. We divide the sky into 192 equal regions of 215 square degrees, and determine p_i , the fraction of particles above v_{\min} with a velocity vector pointing towards bin i . We take the same 100 sample spheres as before, but note that beyond determining sample sphere membership we do not consider the location of a particle: the assignment to a given sky pixel is based solely on the direction of its velocity vector. All of the structure in a given sample sphere is considered *local*, i.e. able to influence the signal at an Earth-bound direct detection experiment.

As an example of the kind of effects high velocity substructure can produce, we show in Fig. 5 the speed distribution $f(v)$ and skymaps for VL2 sample sphere #03. In the halo rest frame (top row, $v_{\min} = 400$ km/s) a very pronounced feature is visible due to the presence of a subhalo moving with galacto-centric velocity modulus of ~ 440 km/s. This feature persists in the Earth rest frame (center row, $v_{\min} = 500$ km/s), where the direction of the subhalo’s motion is “hotter” than the “DM headwind” hotspot in the direction of Earth’s motion. When translating to the Earth’s rest frame, there is an additional degree of freedom arising from the unspecified plane of the Galactic disk. We associate radial motion towards (away from) the Galactic Center with the center (anti-center) of the map, but the hotspot arising from Earth’s motion is free to be rotated around this axis. In this example we have chosen this rotation to maximize the angle between the subhalo hotspot and Earth’s motion. In the bottom row we show for comparison the Earth rest frame map for the MB-case without any substructure.

This is just one strong example, and we would like to understand what sorts of hotspots we might expect. For this purpose we define the hotspot ratio

$$\text{HR}(v_{\min}) = \frac{\max \{p_i(v_{\min})\}}{\max \{p_i^{\text{MB}}(v_{\min})\}}, \quad (3.1)$$

the ratio of the hottest pixel in the sphere sample skymap above v_{\min} to the hottest pixel in the corresponding MB-case, and the hotspot angle ψ between these two pixels. We

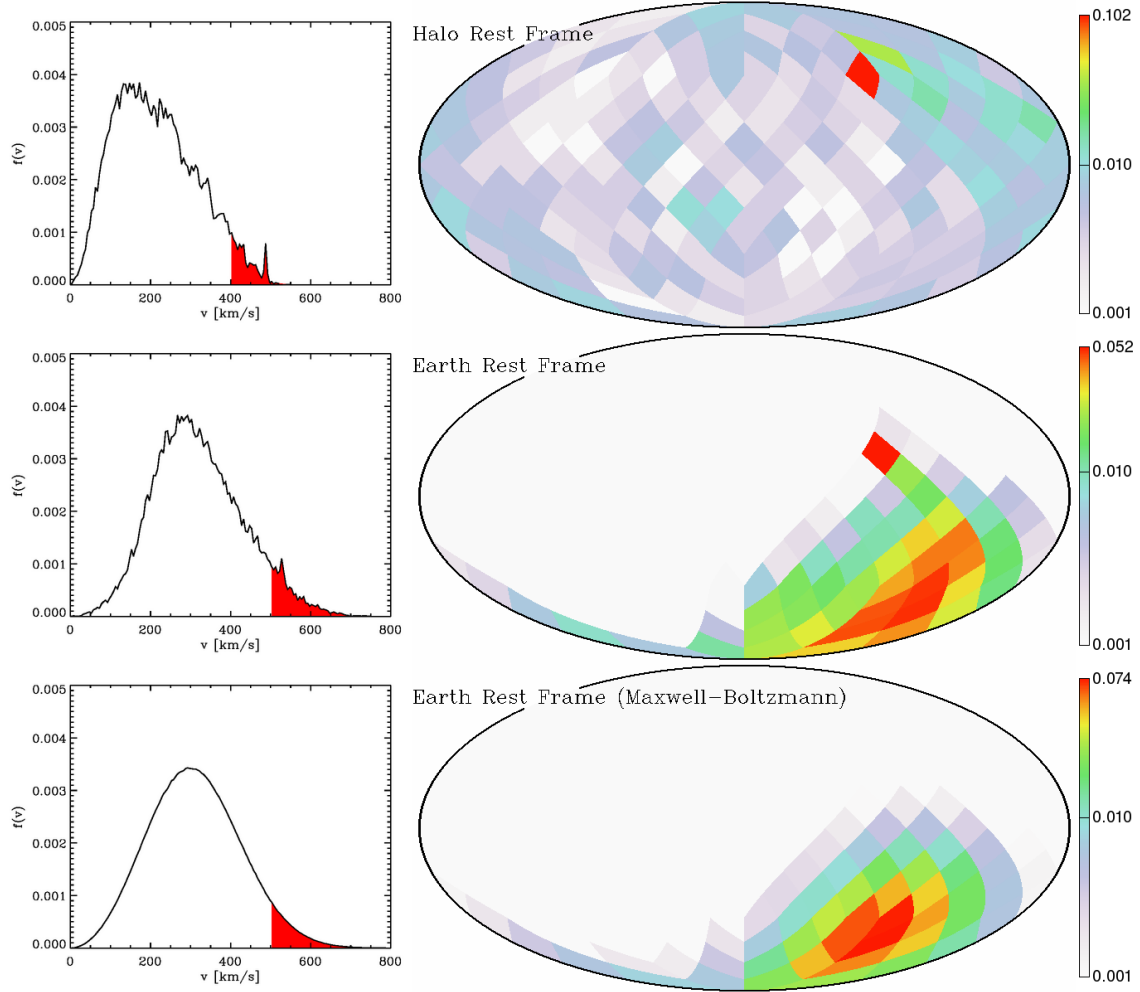


Figure 5: $f(v)$ and HealPix skymaps of the fraction of particles above v_{\min} coming from a given direction, for VL2 sample sphere #03 which contains a fast-moving subhalo. The top row is in the halo rest frame ($v_{\min} = 400$ km/s), and the middle translated into the Earth rest frame ($v_{\min} = 500$ km/s). For comparison the bottom row shows the Maxwell-Boltzmann halo case without substructure.

calculate HR and ψ for all 100 sample spheres, and in each sphere for a full 2π rotation (in one degree increments) of the direction of Earth’s motion. We show in Fig. 6 for VL2 the distribution of HR as a function of v_{\min} and the distribution of ψ for the case without a velocity threshold and for $v_{\min} = 500$ km/s. For small velocities the mean of HR is unity and the r.m.s. variation is only 10%. As v_{\min} increases, HR grows: at $v_{\min} = 600$ km/s, the mean HR is 1.3 ± 0.35 , and at $v_{\min} = 700$ km/s it’s 3.1 ± 1.4 . The downturn at the very highest velocities is caused by running out of particles in the sample spheres. There are also marked changes in the direction of the hottest pixel. Even without a velocity threshold ($v_{\min} = 0$ km/s) in 38% of all cases the direction of the hottest spot on the sky is more than 10° removed from the direction of Earth’s motion (i.e. the MB halo expectation). At

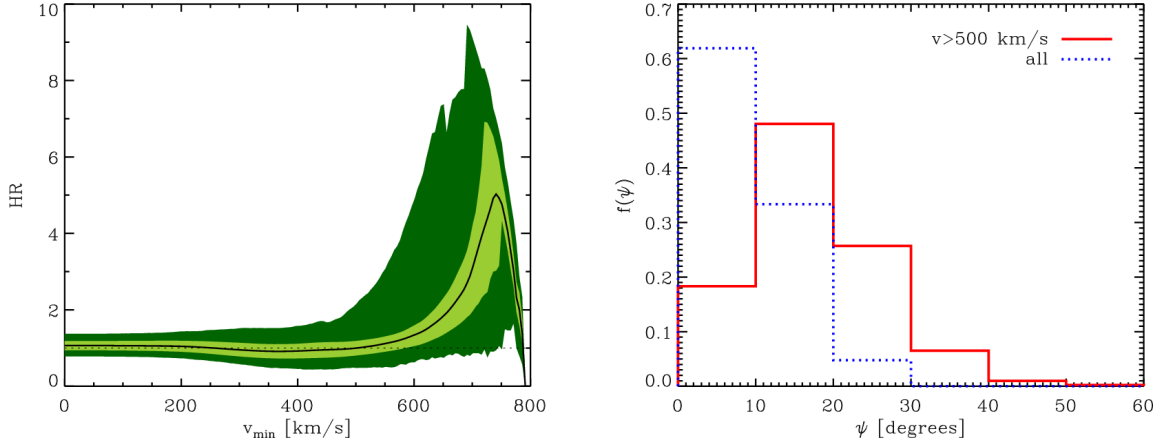


Figure 6: The distribution of $\text{HR}(v_{\min})$ as a function of v_{\min} (*left*) and of ψ for $v_{\min} = 0$ and 500 km/s (*right*) for the VL2 simulation.

$v_{\min} = 500$ km/s the bulk of DM particles are more likely to be coming from a local hotspot with $\psi > 10^\circ$ than from the direction of Earth’s motion. In this case there is only an 18% chance of having $\psi < 10^\circ$. Not all of this structure is due to individual subhalos; some of it may arise from tidal streams, and some from the anisotropic velocity distribution of the host halo particles.

4. Implications for DAMA

In light of the DAMA/LIBRA results [3], two scenarios which have garnered a great deal of attention of late are light dark matter [5, 6], and inelastic dark matter [7, 8]. These scenarios were proposed some time ago to address the conflicts between DAMA [4] and CDMS [40] as well as other experiments at the time.

Recent studies [27, 25, 41, 42] have shown that iDM remains a viable explanation of the DAMA data, consistent with recent results from CDMS [43], XENON10 [44], KIMS [45], ZEPLIN II [46], ZEPLIN III [47] and CRESST [48]. Such models have some tension with CRESST (see the discussion in [27, 49]), which observed 7 events in the tungsten band, while approximately 13 would be expected [27]. While lighter masses have no tension with CDMS, higher mass ($\gtrsim 250$ GeV) WIMPs do.

Light dark matter no longer works in its original incarnation [5, 6], but instead relies upon “channeling,” [50, 51], a difficult to quantify effect whereby some fraction of nuclear recoils have essentially all of the energy converted into scintillation light, rather than just a fraction. Even including channeling, such scenarios seem to have strong tension with the data [52, 24, 53], both in the spectrum of the modulation, and constraints from the unmodulated event rate at low (1-2 keVee) energies³. If one disregards the lowest (2-2.5

³keVee stands for “electron equivalent keV”, a unit of energy used for scintillation light, which is produced by interactions of the recoiling nucleus with electrons. It is related to the full nuclear recoil energy (in keVr) through the quenching factor q : $E(\text{scintillation})/\text{keVee} = q E(\text{recoil})/\text{keVr}$. q is a material-dependent

keVee) bin from DAMA, however, the fit improves [52, 54], but there is still tension for the lightest particles from the presence of modulation above 4 keVee and an overprediction of an unmodulated signal at lower energies. It is important to note that the uncertainties in L_{eff} , the scintillation efficiency of liquid Xenon (see [55] for a discussion), are not completely included in these analyses, and the most recent measurements of L_{eff} [55] suggest that the low energy analysis threshold may be somewhat higher than the 4.5keVr used with $L_{\text{eff}} = 0.19$, weakening the limits. On the other hand, the most recent analysis from XENON10 [56] using a more advanced rejection of double-scatter events shows no events at all in the signal region all the way down to the S2 threshold, strengthening the limits. In light of these uncertainties, and in view of the importance of the result, we believe it is best to maintain an open mind about the viability of the light WIMP explanation.

For our purposes, the crucial feature is that these scenarios sample the high ($v \sim 600$ km/s) component of the velocity distribution, and so are especially sensitive to the departures from a simple Maxwell-Boltzmann distribution. Consequently, it is important to investigate whether these changes affect the tensions described above.

4.1 Inelastic Dark Matter

The inelastic Dark Matter scenario [7] was proposed to explain the origin of the DAMA annual modulation signal. The scenario relies upon three basic elements: first, the presence of an excited state χ^* of the dark matter χ , with a splitting $\delta = m_{\chi^*} - m_{\chi} \sim m_{\chi}v^2$ comparable to the kinetic energy of the WIMP. Second, the absence of, or at most a suppressed elastic scattering cross section off of nuclei, i.e., the process $\chi N \rightarrow \chi N$ should be small. Third, an allowed cross section for inelastic scatterings, i.e., $\chi N \rightarrow \chi^* N$, with a size set roughly by the weak scale.

Although these properties may seem odd at first blush, they are in fact perfectly natural if the scattering occurs through a gauge interaction [7, 8], where the splitting is between the two Majorana components of a massive pseudo-Dirac fermion, or between the real and imaginary components of a complex scalar. Simple models can be constructed where the mediating interaction is the Z-boson [7, 8, 57, 41]. Models with new vector interactions to explain the PAMELA positron excess also naturally provide models of iDM [58], and often where all scales arise naturally from radiative corrections [58, 59, 60, 61, 62]. Composite models provide a simple origin for the excited states as well [63, 64].

The principle change is a kinematical requirement on the scattering,

$$\beta_{\text{min}} = \sqrt{\frac{1}{2m_N E_R} \left(\frac{m_N E_R}{\mu} + \delta \right)}, \quad (4.1)$$

where m_N is the mass of the target nucleus and μ is the reduced mass of the WIMP/target nucleus system. For $\delta \sim \mu\beta^2/2$, the consequences can be significant. This requirement has three principal effects: first, the kinematical constraint depends on the target nucleus mass, and is more stringent for lighter nuclei. If we are sampling dominantly the tail of the velocity distribution, the relative effect between heavy and light targets (e.g., iodine versus quantity that must be experimentally determined.

germanium) can be significant. Second, again because the signal is sampling the tail of the velocity distribution, the modulated amplitude can be significantly higher than the few percent expected for a standard WIMP. In fact, in the cases where there are particles kinematically scattering in the summer, but not the winter, the modulation can reach 100%. Third, the inelasticity suppresses or eliminates the event rate at lower energies. Because standard WIMPs have exponentially more events at lower energies, most experiments have focused on controlling background in this region and lowering the threshold. In particular, the XENON10 and ZEPLINI experiments have few events at low energies, but a significant background at higher energies. Consequently, their limits for standard WIMPs are quite strong, but significantly weaker for inelastic WIMPs. The combination of these three elements allows an explanation of the DAMA result that is consistent with all other current experiments [27, 25, 41].

4.1.1 Fitting the DAMA signal

DAMA reports an annual modulation in the range of 2 – 6 keVee range. This can be interpreted as arising from either Na or I scattering events. In the former case (Na), it has been shown that the “light inelastic” region (an approximately 15 GeV WIMP with $\delta \approx 30$ keV) can open up significant parameter space [52, 49]. In the latter case (I), we find the “heavy inelastic” region (a 100+ GeV WIMP with $\delta \gtrsim 100$ keV) opens significant parameter space. Since the constraints are stronger on the heavy case, we focus on this region.

When determining the precise values of parameters that might agree with DAMA, we must convert from keVee to keVr, which already introduces significant uncertainties, a point which has been recently discussed by [25]. The quenching factor for iodine has been found to have a range of different values, including $q = 0.09 \pm 0.01$ [65], $q = 0.05 \pm 0.02$ [66], $q = 0.08 \pm 0.02$ [67] and $q = 0.08 \pm 0.01$ [68]⁴. The first two measurements of the quenching factor are somewhat indirect, fitting event distributions at low energies. The last two are more direct. Of the last two, we should note that the first includes non-linearity in its stated uncertainty, while the second explicitly fixes to a signal electron energy, and thus this effect is not included. We adopt $q = 0.08 \pm 0.02$ as the value for quenching, which corresponds to a range of 25 – 75 keVr for DAMA.

4.1.2 Constraining the iDM interpretation of DAMA

While iDM allows DAMA to exist consistently with the other experiments, the reach of other experiments is at or near the predicted DAMA level. In particular, as we see in Fig. 14, within the context of a MB halo, at high masses, CDMS excludes the entire range of the parameter space that fits DAMA. At the same time, the CRESST results (with a tungsten target) seem very tense with the data over the whole mass range. These two experiments provide the greatest present tension with the iDM interpretation of DAMA. An

⁴The value quoted by [68] is generally $q = 0.086 \pm 0.007$, but this value averages over a wide range of energies. The two measured values for the DAMA energy range specifically are $q = 0.08 \pm 0.01$ and $q = 0.08 \pm 0.02$.

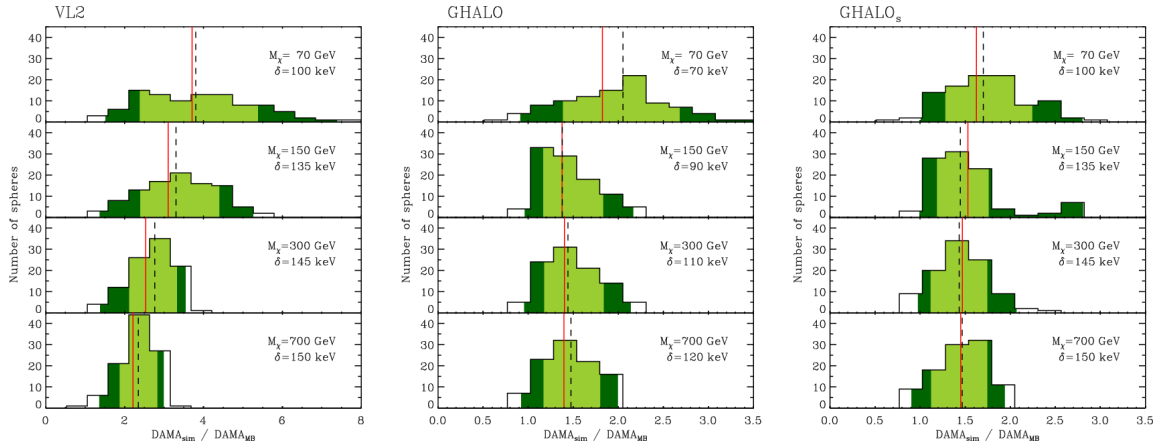


Figure 7: The ratio of DAMA signal in a given simulation to that in a MB distribution. The solid red line is the spherical shell average, the dashed line the median of the distribution over the sample spheres.

immediate question we can ask is then whether the velocity-space distribution of particles in the simulations makes the constraints more or less significant than a MB distribution.

This is not an easy question to answer. Since there can be significant spatial variation in the velocity distribution, we would like to quantify this without making full exclusion plots for every data point. The three principle constraints on the iDM interpretation of DAMA come from a) Xe experiments (XENON10, ZEPLIN-II and ZEPLIN-III), b) CDMS (Germanium) and c) CRESST (Tungsten). While varying the halo model can have significant effects on each experiment, including rates and spectra, the variation of velocity structures in the different halos affects these limits differently, and it is difficult to quantify in aggregate what the effects are.

Before proceeding into a detailed analysis of the DAMA signal, we can already study a preliminary question: how does the cross section needed to explain DAMA compare between a MB halo and a simulation? We consider the ratio of the modulation between MB and the simulations in Fig. 7. Overall, we see that the signal at DAMA is *increased* in the simulation, as much as a factor of a few.

Of course, increasing the DAMA signal does not change the constraints if the signal in any of the other experiments is changed, as well. We proceed by next considering a ratio of ratios (RoR). Since Germanium (CDMS) has a higher velocity threshold than Iodine (DAMA), while Tungsten (CRESST) has a lower velocity threshold, a simple test is to look at the variation of the signal at different experiments as a fraction of the DAMA modulation amplitude. We thus calculate for each of the simulation samples (spherical shell and 100 spheres), as well as for the best-fitting MB model, the ratios of the CDMS and CRESST signals, integrated from 10-100 keV, to the total DAMA modulation in either of the high- q and low- q benchmark regions described above. We then divide the simulation ratio by the MB ratio: $(\text{CDMS}/[\text{DAMA}])_{\text{sim}}/(\text{CDMS}/[\text{DAMA}])_{\text{MB}}$ and $(\text{CRESST}/[\text{DAMA}])_{\text{sim}}/(\text{CRESST}/[\text{DAMA}])_{\text{MB}}$. If these RoR's are smaller than one,

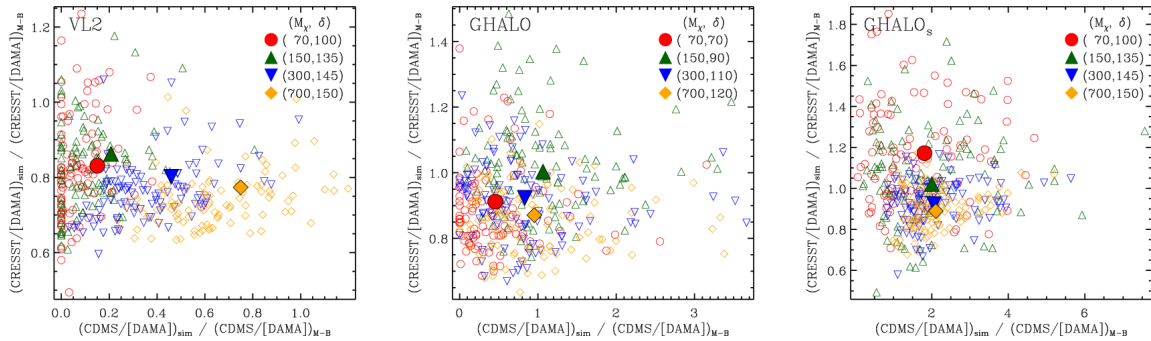


Figure 8: Scatter plots of the ratios of ratios (RoR, see text for details) for the CRESST and CDMS experiments. RoR’s less than one indicate that using the simulation’s velocity distribution instead of the best-fitting MB model weakens the CRESST or CDMS limits relative to the DAMA (high- q) signal.

it suggests that using the simulation’s velocity distribution instead of the best-fitting MB distribution weakens the limits relative to DAMA, while values larger than one imply stronger limits. The effects on Xenon limits are harder to quantify, because of the added uncertainties in the conversion from keVee to keVr at those experiments, and where, precisely, the backgrounds lie. Thus, we consider first only CDMS and CRESST limits.

In Fig. 8 we show scatter plots of the CRESST RoR against the CDMS RoR. Large filled symbols indicate the spherical shell sample and small symbols are used for the sample spheres. Note that in some cases the CDMS RoR is zero, indicating that the simulation velocity distribution resulted in no CDMS signal at all. A few things are immediately obvious from this plot. First, the limits from CDMS can vary wildly between simulations, and even between different spheres within a single simulation. This simply represents how dramatically the velocity distribution can change at the highest velocities. Second, we see that the CRESST rate is much more weakly affected, with typical suppressions of (0.6-1), (0.7-1.1), and (0.7-1.3) for Via Lactea II, GHALO and GHALO_s respectively. Thus, from the perspective of Poisson limits, these results would suggest that those derived from Maxwellian halos are possibly excessively aggressive by almost a factor of two. However, many limits are placed using one of Yellin’s techniques [69], where not only the overall rate, but also the distribution of signal versus background is important. Here we find that the halo uncertainties can be at their largest. We show in Fig. 9 the spectra at DAMA and CRESST for a 100 GeV WIMP with $\delta = 130, 150, 170$ keV. We employ energy smearing at DAMA by assuming that the smearing reported for the one of 25 targets of DAMA/LIBRA [70] is characteristic of all of them. We assume a smearing of 1 keV at CRESST.

One can see that the peak positions and properties can change by quite a large amount. At DAMA, the effect of this is principally to shift the peak. Such an effect is largely degenerate with the quenching uncertainty, which can reasonably range from $q = 0.06$ to $q = 0.09$. (For a lower quenching value, for instance, the peak will shift to lower energy in keVee.) The effects would be similar at XENON10, where the energy smearing will eliminate most interesting structures, and the shift in the location of the peak will be

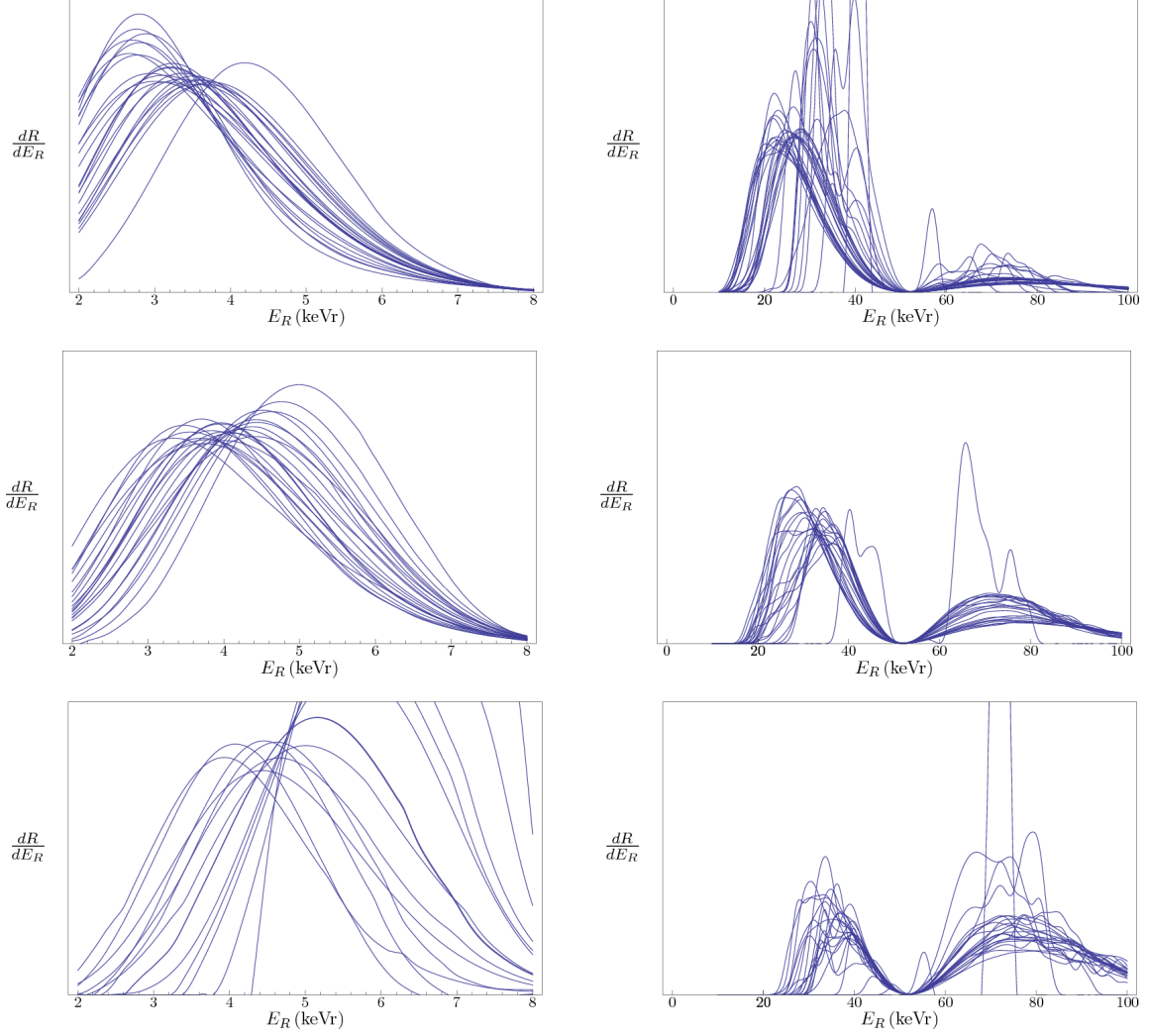


Figure 9: *Left:* The differential recoil energy distribution (in $\text{dru}=\text{events}/\text{kg}/\text{day}/\text{keV}$) at DAMA for selected spheres from VL2, GHALO and GHALO_s, normalized to unity in the DAMA signal range 2-6 keVee *Right:* The distribution at CRESST for the same spheres, normalized to unity from 0-100 keV. The models are $m_\chi = 100$ GeV and $\delta = 130$ (top), 150 (middle), 170 (bottom) keV.

comparable to the uncertainties induced from L_{eff} . In contrast, the spectrum for CRESST can vary *dramatically*, with the peak location moving from below 30 keV to above 60 keV. The implication of this is that techniques such as optimum interval, maximum gap and p_{max} are likely all overly aggressive in that a peak in the spectrum might arise at a specific location in the real Milky Way halo, but that would not be reproduced at the appropriate position, for instance in a Maxwellian halo. In general, any technique that relies on knowing precisely the predicted spectrum is unreliable when considering these variations.

Although we are still limited by our sample of simulations, we can study the effects on various limits by looking at the allowed parameter space and limits in a variety of halos. To do so, we largely follow [27] in calculating the allowed parameter space and limits, with

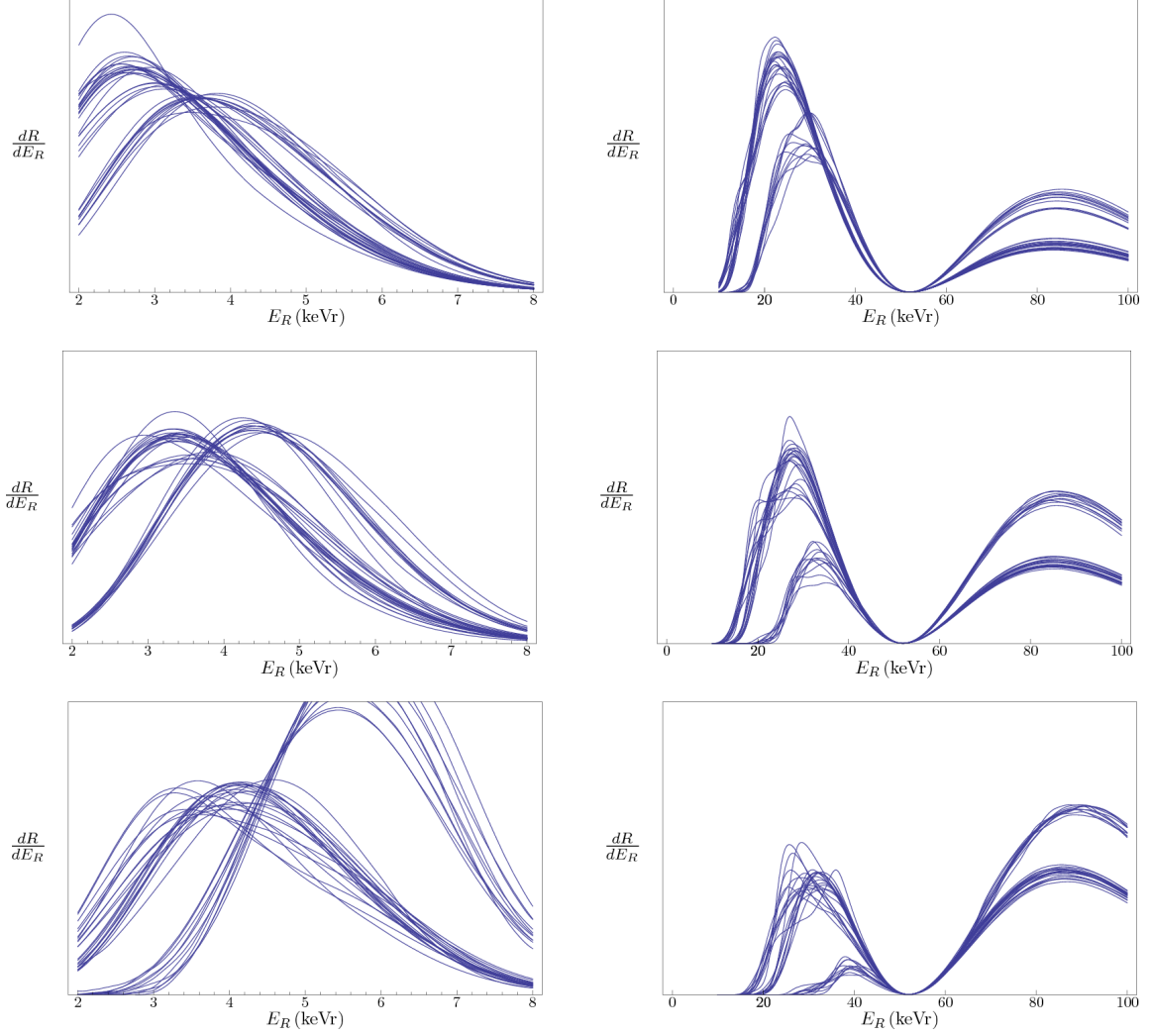


Figure 10: As in Fig. 9, but with $m_\chi = 700$ GeV.

a few important differences. As pointed out by [25], the uncertainty in quenching factor for iodine can be extremely important. We thus consider the range $q = 0.06$ to $q = 0.09$ and take the 90% allowed region to be the union of 90% allowed regions, and similarly for the 99% region. We smear the signal as described above.

For CDMS we employ the maximum gap method with the data set specified in [27].

For limits arising from XENON10, we use the data presented in the recent reanalysis of [56], and calculate the maximum gap limit (as in ZEPLIN-II and ZEPLIN-III) for both [71] and [55] values of L_{eff} , taking at every point the more conservative of the two. For limits, we employ the maximum gap method. Since the data are smeared and there are great uncertainties in L_{eff} , the detailed spectral information arising from structure is lost.

For ZEPLIN-II, we take the data described in [46], but (conservatively) take the energy values to be shifted by a factor of 0.24/0.19 for a maximum gap analysis, which employs

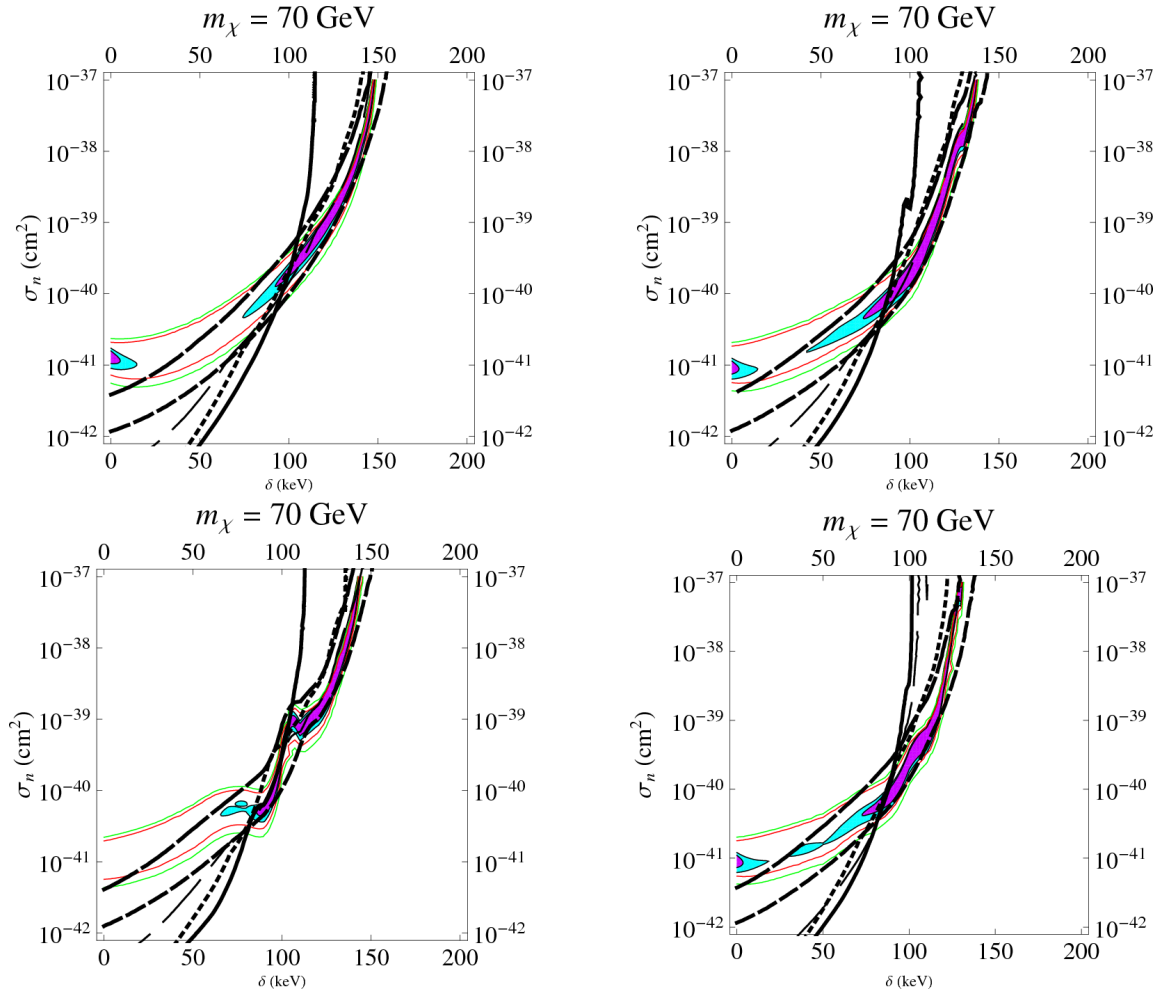


Figure 11: Allowed parameter space for DAMA at 90% (purple) and 99% (blue) with $m_\chi = 70$ GeV. For comparison the 90% and 99% regions for DAMA/LIBRA rates only (as opposed to DAMA/NaI + DAMA/LIBRA) are shown in red and green lines. Constraints are CDMS (solid), ZEPLIN-III (long dashed, thin), ZEPLIN-II (long-dashed, thick), CRESST (medium-dashed) and XENON10 (short-dashed). The regions are MB with $v_0 = 220$ km/s and $v_{\text{esc}} = 550$ km/s (*top left*), VL2 (*top right*), and a sample sphere from VL2 (*bottom, left*) and GHALO_s (*bottom, right*).

the value of L_{eff} from [71] at higher energies.⁵

For ZEPLIN-III, we utilize the data within the published acceptance box up to 15 keVee for the maximum gap analysis. We additionally employ data outside the blind acceptance box up to 30 keVee, the maximum to which efficiencies were provided in [47]. We use the delineated 1σ region for the data in this high energy range since the 3σ region is not specified. To convert from keVee to keVr, we use

$$E_r = (0.142E_{\text{ee}} + 0.005) \exp(-0.305 E_{\text{ee}}^{0.564}) \quad (4.2)$$

⁵We could parameterize L_{eff} as a function of energy, and use different shifts at different energies, but the limits are essentially the same, being dominated by the events at the highest energy.

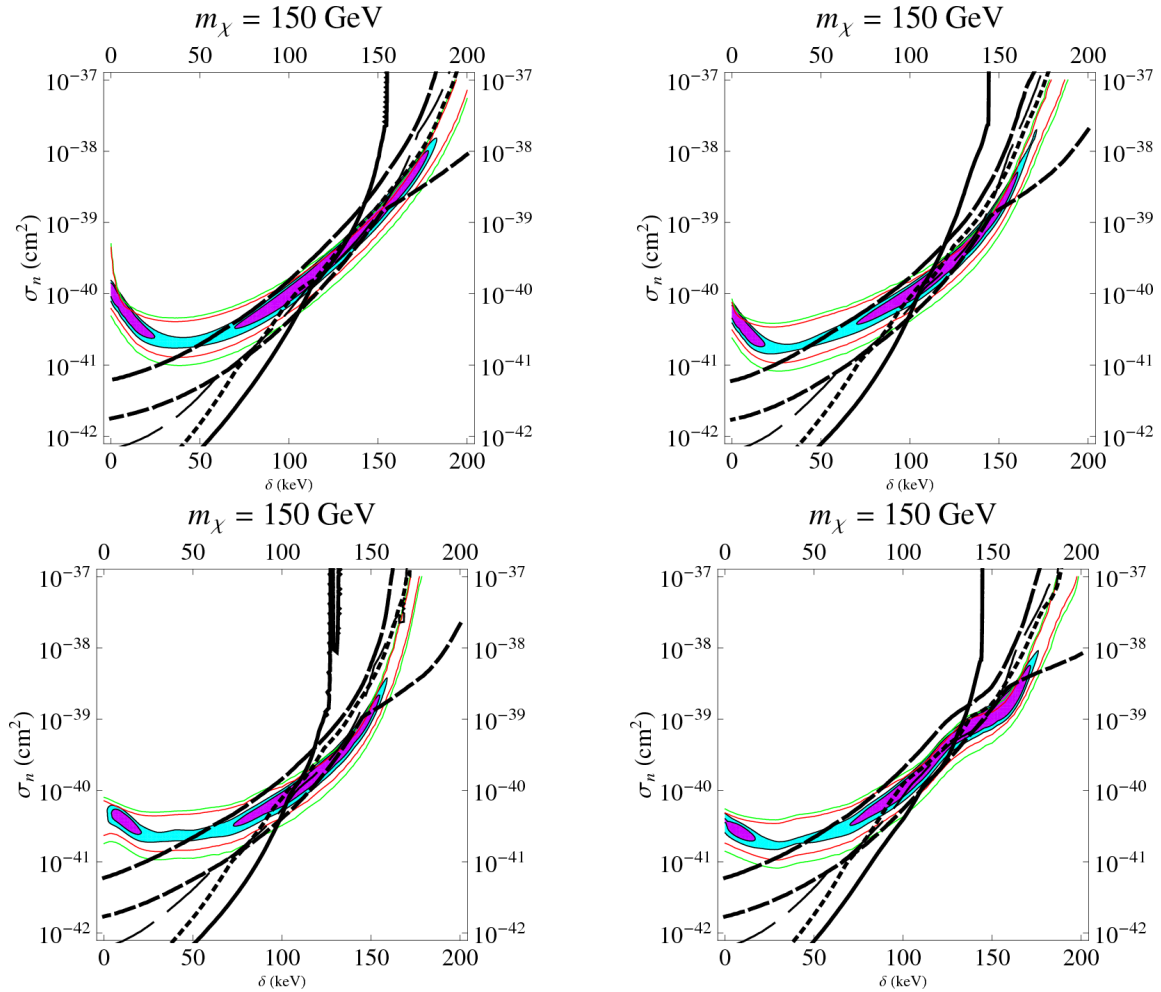


Figure 12: As in 11, but with $m_\chi = 150$ GeV.

below 10 keVee [25, 42], and a constant ratio of 0.55 above that. (We use a larger value than [42] at high energies to account for the energy dependent value of L_{eff} suggested by [71], which tends to weaken limits slightly.) Note that we do not employ a background subtraction using the science data as in [72], nor do we do so for ZEPLIN-II as the same basic technique seems to have led to a significant overprediction of background for ZEPLIN-III.

For all Xe based experiments, we take a fixed smearing of $\sqrt{30}$ keVr, which is typical of the smearing of the experiments in the range of the peak signal.

For the CRESST experiment, we consider the data from the commissioning run [48], as well as the additional events at ~ 22 keV, 33 keV and 88 keV presented for Run 31 by [73], and take a smearing of 1 keV. As described above, Yellin-style techniques are ironically inappropriate for experiments with high energy resolution. Because of the significant variation in the possible spectrum when varying halo models with the high energy resolution, we use a binned Poisson analysis, rather than a maximum-gap technique.

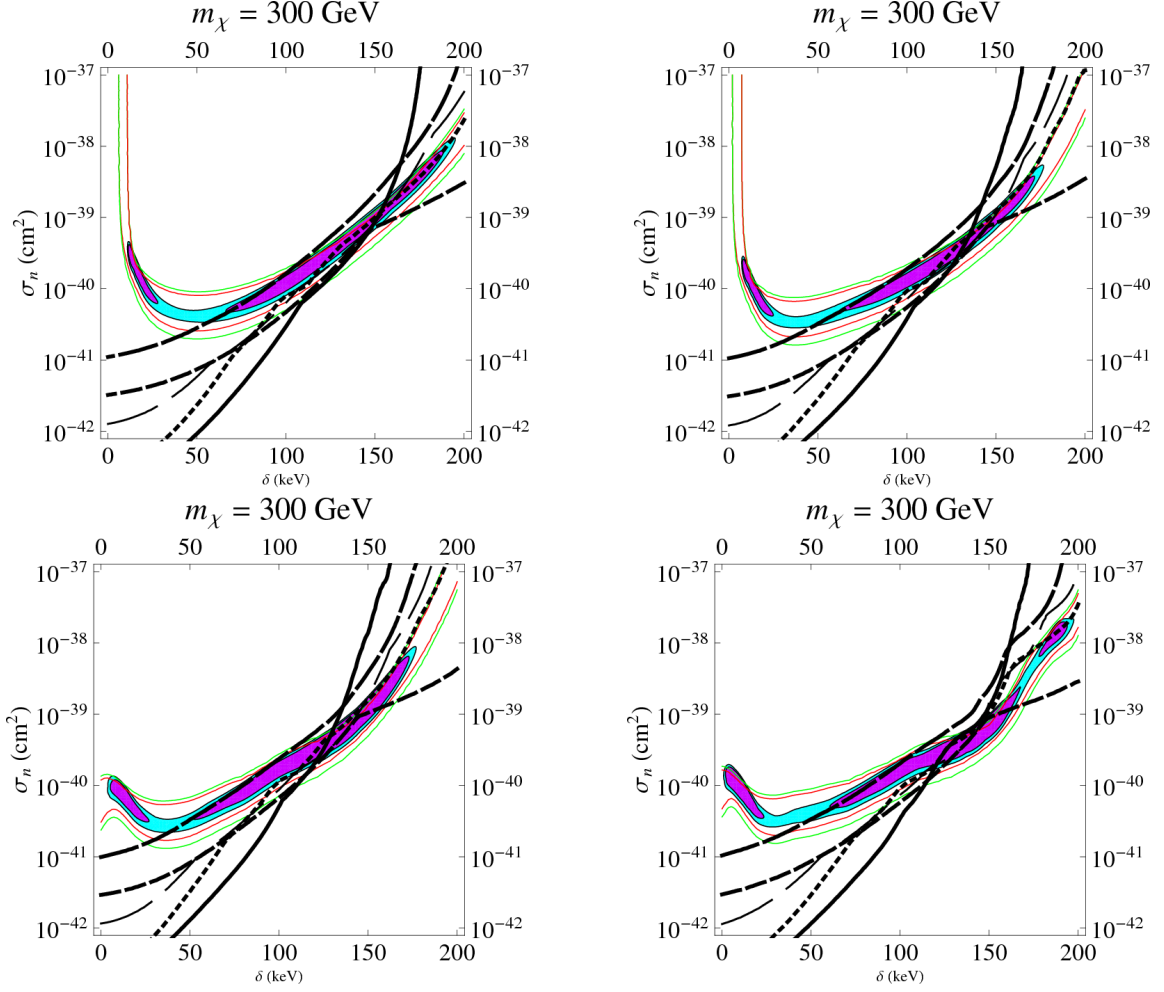


Figure 13: As in 11, but with $m_\chi = 300$ GeV.

We divide up the signal region into a low region ($E_R < 35$ keV), a middle region ($35 \text{ keV} < E_R < 50$ keV) and a high region ($50 \text{ keV} < E_R < 100$ keV). In this way, we do not overweight the events near the zero of the form factor (in the mid region), but still include some broad spectral information. We require that the rate be lower than 95% Poisson upper limits for each bin, which is a 95% limit when the signal is exclusively in the low bin and $\sim 90\%$ when there is signal in both the low and high bins, and $\sim 85\%$ in the (rarer) instances when there is signal in all three bins. Although stronger limits can be set using for instance, optimum interval, because of the uncertainties in the halo distribution, this seems inappropriate. In other words, if some of the events at CRESST are real, then the distribution of events may well be telling us the properties of the halo.

We show the results of these limits in Figs. 11-14. Even when accounting for smearing, and using a binned Poisson limit instead of optimum interval, it is remarkable how significantly the allowed parameter space can change from simulation to simulation, and between spheres in the same simulation. We see that CRESST remains the most constraining, as

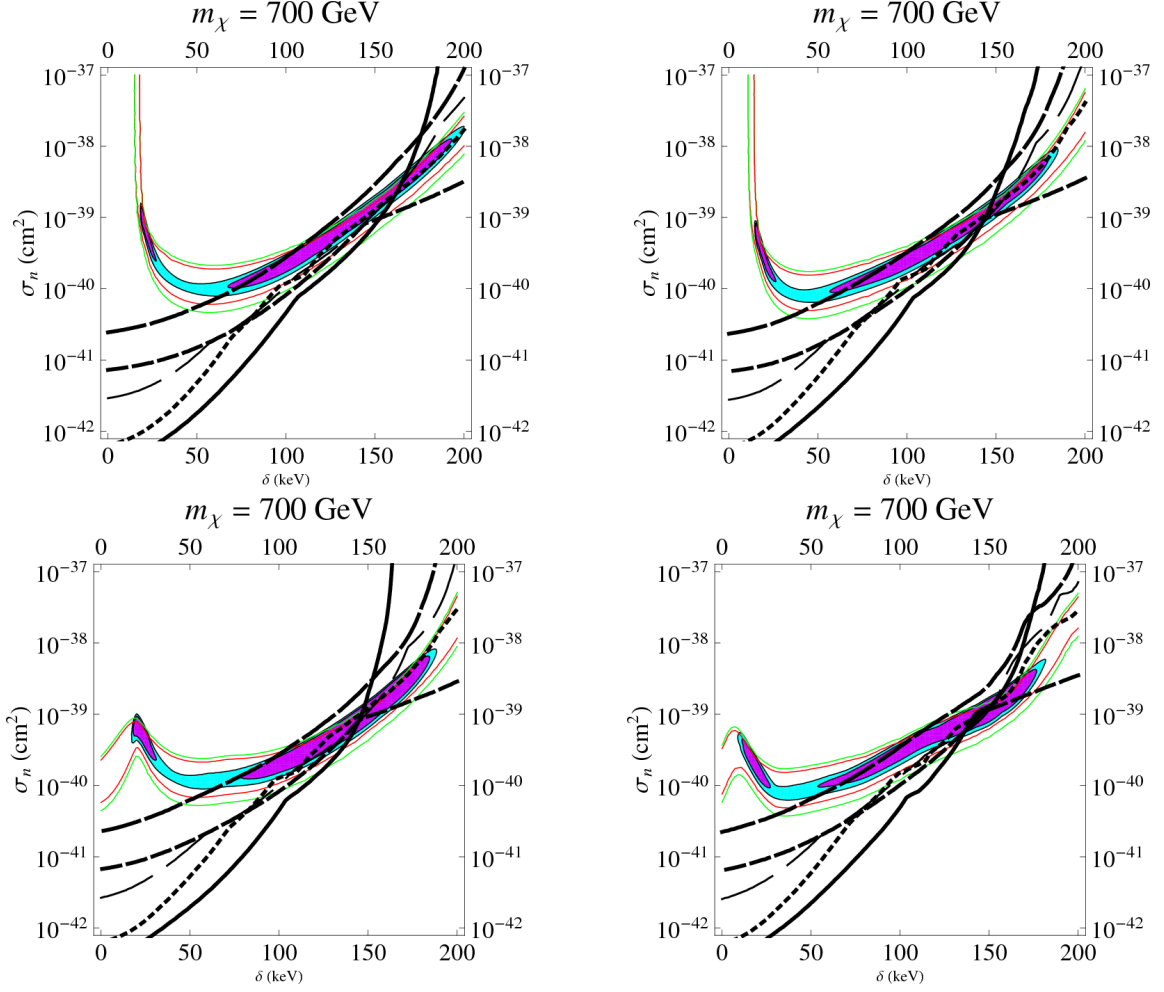


Figure 14: As in 11, but with $m_\chi = 700$ GeV.

found previously, but we see important differences. First, agreement is generally improved in these spheres. This is due to the presence of structure at high velocities which increases the modulated fraction at DAMA. As a consequence, small regions of allowed parameter space exist at high mass, the size of which depends significantly on the particular halo. Larger regions exist at smaller mass (~ 150 GeV). Moreover, the allowed region of parameter space can shift dramatically in σ and δ , with pockets appearing at large δ from high velocity particles. Should iDM be relevant for nature, the detailed nature of the halo is clearly significant in determining the properties of the direct detection signals.

4.2 Light dark matter

Light (\sim GeV) dark matter [5] has been proposed as a means to reconcile DAMA with the other existing experiments [6, 74, 51]. The current iteration of LDM involves “channelling” [75, 50] whereby for some small fraction of the time the entirety of the nuclear recoil energy is converted to scintillation light. Since the observed energy is lower, it allows lighter

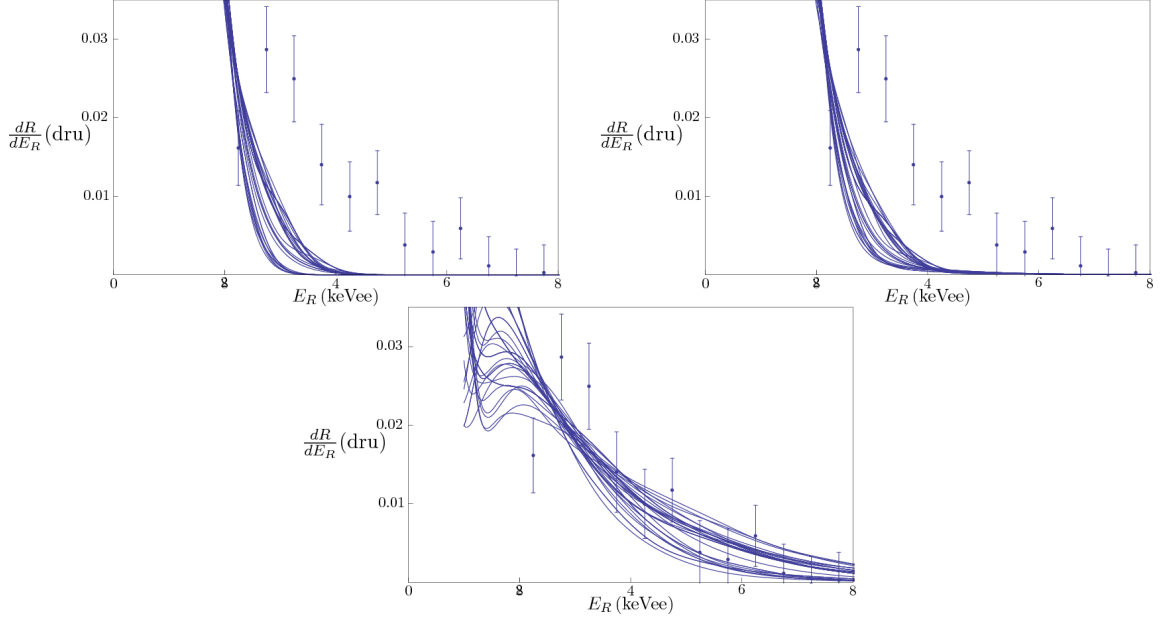


Figure 15: Spectra for a sample of spheres best fit to the DAMA data (shown) within the different simulations for LDM models with $m_\chi = 3$ GeV (*top, left*), 7 GeV (*top, right*), and 13 GeV (*bottom*).

WIMPs to scatter at the DAMA experiment. Such light WIMPs may be incapable of depositing energy above the threshold at XENON10 or CDMS-Si, for instance, allowing DAMA to evade these bounds.

Such an explanation is not without difficulty, however. These light WIMPs have a rapidly falling event spectrum, due to the decreasing probability of channeling at higher energies, and the increasingly suppressed number of particles with higher kinetic energy. As a consequence the spectrum of LDM seems generally to fall too rapidly at light masses [52, 24, 53]. At higher masses, the spectrum is acceptable, but is excluded by other experiments. We should note again here that this is under the assumption that the errors in the data are statistical only. Should there be, e.g., significant changes in the efficiency, it is possible that LDM could give a better fit. As noted earlier, the uncertainties in L_{eff} should weaken these limits, while the most recent analysis from XENON10 (with no events to the S2 threshold) would strengthen the limits. Thus, while the models do not seem to describe the data well, there are adequate uncertainties that this scenario remains an interesting possibility as an explanation of the DAMA signal.

Since these models are also extremely sensitive to the presence of high velocity particles, one might wonder whether, just as in the iDM case, the properties of halos at high velocities might modify the spectrum and the relative signal strength at other experiments.

We begin again by addressing the question of the effects on the spectrum. We show these for three different masses in Fig. 15. One can see that, while there are noticeable changes in the spectrum, its overall shape remains basically unchanged. The difference between LDM and iDM here is simple: in iDM, the “threshold” (i.e., minimum velocity)

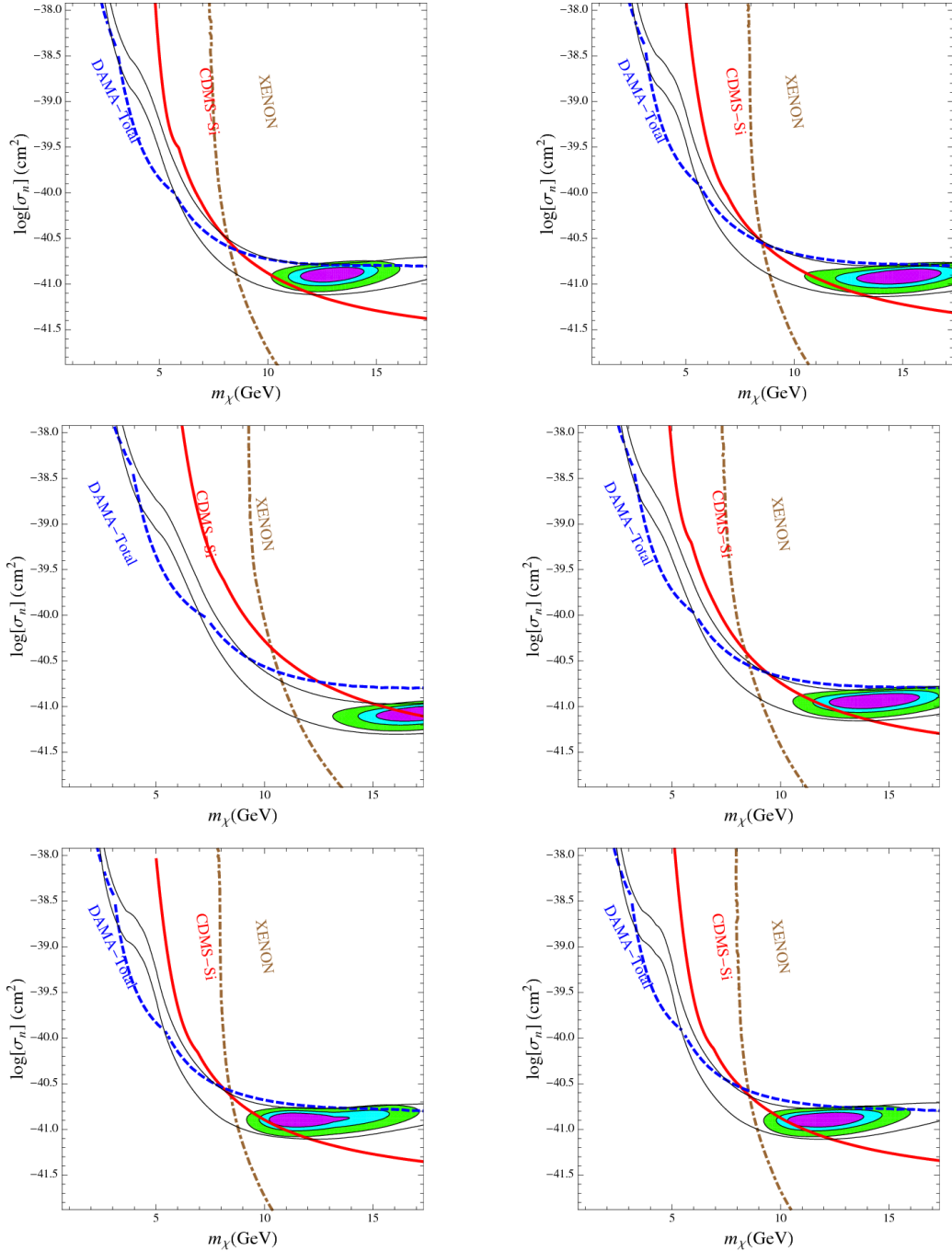


Figure 16: The allowed parameter space for LDM models. *Top, left:* MB with $v_0 = 220$ km/s and $v_{\text{esc}} = 550$ km/s. *Top, right:* VL2. *Middle, left:* GHALO. *Middle, right:* GHALO_s. *Bottom two* sample spheres taken from the simulations.

scattering is actually at large energy, and to go to lower energies one requires *higher* velocities. Competing against this are the significant form factor effects. The competition between these two sensitive quantities leads to dramatic changes and features. For LDM, the threshold scattering is at zero, and all effects (channeling, form factor, velocity dis-

tribution) contribute to the falling (unmodulated) spectrum. Thus, it can fall somewhat more or less rapidly, depending on the number of particles at high velocity, but without very significant changes.

To determine the spectrum, we follow the analysis of [52]. The most proper analysis would be to include the updated measurement of L_{eff} (which will weaken the limits) and the reanalysis to remove multi-hit events from [56] (which strengthens the limits). However, incorporating the S2 threshold, resulting in contribution to an energy-dependent acceptance at low energies is complicated. Lacking detailed information on this, we will restrict ourselves to the previous XENON10 limits. Since our point is the relative change from halo model to halo model, this is reasonable, so long as we recognize that the limits should be taken with a grain of salt.

We show in Fig. 16 the allowed parameter space for the LDM scenario for the canonical MB model, for the (averaged) simulations VL2, GHALO and GHALO-scaled, as well as two sample spheres from the halos. We see that the small spectral effects translate into small effects in the allowed parameter space. There can be some improvement, however, and although the exclusion curves technically cover the allowed regions, uncertainties in the low-energy scintillation of Xe, for instance, and the ambiguity of employing statistical errors without a covariance matrix suggest that a small region may yet be allowed near 10 GeV. We should again emphasize that there is no sense in which the sampling we have done is statistically complete, and our failure to find an allowed region does not preclude the possibility that one exists, or might arise in another simulation. A proper reanalysis using the data from [56] is warranted.

5. Discussion

Direct detection of dark matter intimately ties up questions of astrophysics and particle physics. In recent years, the range of particle physics models has exploded, many with new interactions and properties. Some of these, in particular light dark matter and inelastic dark matter, are particularly sensitive to the high velocity tail of the WIMP velocity distribution. The same is true, even for standard WIMPs, for many directionally sensitive detection experiments (e.g. DRIFT, NEWAGE, DMTPC), which rely on high recoil energies in order to measure the direction of the scattering DM particle. It is especially at these high velocities that deviations from the standard isothermal Maxwell-Boltzmann assumption are expected to be most significant. Velocity substructure, arising from nearby subhalos and tidal streams, as well as from the host halo’s velocity anisotropy, can have profound effects on the expected event rates, the recoil energy spectrum, and the typical direction of scattering DM particles.

We have studied the effects of these deviations by employing data from N-body simulations directly, rather than with analytic fits that miss interesting structures. Our analysis is based on two of the highest resolution numerical simulations of Galactic dark matter structure, Via Lactea II and GHALO. We confirm previously reported global departures from the Maxwell-Boltzmann distribution, with a noticeable excess of particles on the high

velocity tail. In many of our local samples we find additional discrete features due to subhalos and tidal streams.

These global and local departures from the standard Maxwellian model have a number of interesting consequences:

- For directionally sensitive detection, we have found that the fraction of particles coming from the “hottest” direction in the sky increases with the velocity threshold. More importantly, the direction from which most DM particles are coming can be affected significantly. At high velocity thresholds ($\gtrsim 500$ km/s in the Earth’s frame) the typical direction is more often than not shifted by $> 10^\circ$ away from the direction of Earth’s motion, and up to 80° in extreme cases.
- For inelastic DM the effects are dramatic. The relative strength of CDMS limits versus DAMA can change by an order of magnitude, while the relative strength of CRESST limits can change by almost a factor of two. For CRESST most of this effect is due to an enhanced modulation, which can be a factor of two larger than for a Maxwellian halo. Such effects would persist at Xenon detectors as well, changing their sensitivity relative to DAMA by $\mathcal{O}(1)$.
- For light DM, we have seen that small changes in the spectrum are possible, although not so much as to allow very light (~ 1 GeV) WIMPs to fit the existing data, but only somewhat heavier ($\gtrsim 10$ GeV).
- In general, dramatic variations in the spectrum can appear for iDM models, complicating attempts to employ Yellin-type analyses, which rely upon a detailed knowledge of the predicted spectrum of the model. Instead we advocate a binned Poisson analysis, which is less sensitive to assumption about the shape of the signal spectrum.
- A further important effect that we have found is the possible variation of the phase of modulation as a function of energy. This has been noted before in the context of streams [76]. Since most background modulations would be expected to have the same phase as a function of energy, such a change could be a strong piece of evidence that a modulated signal was arising from DM.

It is important to keep in mind that our simulations are nowhere close to resolving the phase-space structure at the relevant sub-parsec scales, and we rely on extrapolation from a coarser sampling (1-1.5 kpc radius spheres). If velocity substructure does not persist on smaller scales, then our analysis may overestimate the likelihood of these effects. On the other hand, we are probably underestimating the significance of the effects, since at the moment we are diluting the substructure signal by the host halo particles, while it would completely dominate the background host halo, should the Earth be passing through one of these substructures.

We have seen here how, should DM be conclusively discovered with direct detection experiments, it may begin to help unlock questions about the formation of the galaxy, precisely *because* of these dramatic sensitivities. With the fantastic improvements in direct

detection on the horizon it is more important than ever to increase our awareness of the significant impact that the detailed structure of our Galaxy's dark matter halo may have.

Acknowledgments

The authors thank S.Chang and A.Pierce for discussions and their collaboration in the development of the DM direct detection analysis tools. MK gratefully acknowledges support from William L. Loughlin at the Institute for Advanced Study, and from the Theoretical Astrophysics Center at UC Berkeley. NW is supported by DOE OJI grant # DE-FG02-06ER41417 and NSF CAREER grant PHY-0449818.

References

- [1] F. J. Kerr and D. Lynden-Bell, *Review of galactic constants*, *Mon. Not. Roy. Astron. Soc.* **221** (1986) 1023.
- [2] M. Kamionkowski and A. Kinkhabwala, *Galactic halo models and particle dark matter detection*, *Phys. Rev.* **D57** (1998) 3256–3263, [[hep-ph/9710337](#)].
- [3] **DAMA** Collaboration, R. Bernabei *et al.*, *First results from DAMA/LIBRA and the combined results with DAMA/NaI*, *Eur. Phys. J.* **C56** (2008) 333–355, [[arXiv:0804.2741](#)].
- [4] **DAMA** Collaboration, R. Bernabei *et al.*, *Search for WIMP annual modulation signature: Results from DAMA / NaI-3 and DAMA / NaI-4 and the global combined analysis*, *Phys. Lett.* **B480** (2000) 23–31.
- [5] A. Bottino, F. Donato, N. Fornengo, and S. Scopel, *Light neutralinos and WIMP direct searches*, *Phys. Rev.* **D69** (2004) 037302, [[hep-ph/0307303](#)].
- [6] P. Gondolo and G. Gelmini, *Compatibility of DAMA dark matter detection with other searches*, *Phys. Rev.* **D71** (2005) 123520, [[hep-ph/0504010](#)].
- [7] D. R. Smith and N. Weiner, *Inelastic dark matter*, *Phys. Rev.* **D64** (2001) 043502, [[hep-ph/0101138](#)].
- [8] D. Tucker-Smith and N. Weiner, *The status of inelastic dark matter*, *Phys. Rev.* **D72** (2005) 063509, [[hep-ph/0402065](#)].
- [9] J. Diemand, M. Kuhlen, and P. Madau, *Dark matter substructure and gamma-ray annihilation in the Milky Way halo*, *Astrophys. J.* **657** (2007) 262, [[astro-ph/0611370](#)].
- [10] J. Diemand *et al.*, *Clumps and streams in the local dark matter distribution*, *Nature* **454** (2008) 735–738, [[arXiv:0805.1244](#)].
- [11] J. Stadel, D. Potter, B. Moore, J. Diemand, P. Madau, M. Zemp, M. Kuhlen, and V. Quilis, *Quantifying the heart of darkness with GHALO - a multibillion particle simulation of a galactic halo*, *MNRAS* **398** (Sept., 2009) L21–L25, [[arXiv:0808.2981](#)].
- [12] V. Springel, J. Wang, M. Vogelsberger, A. Ludlow, A. Jenkins, A. Helmi, J. F. Navarro, C. S. Frenk, and S. D. M. White, *The Aquarius Project: the subhaloes of galactic haloes*, *MNRAS* **391** (Dec., 2008) 1685–1711, [[arXiv:0809.0898](#)].
- [13] M. Zemp, J. Diemand, M. Kuhlen, P. Madau, B. Moore, D. Potter, J. Stadel, and L. Widrow, *The graininess of dark matter haloes*, *MNRAS* **394** (Apr., 2009) 641–659, [[arXiv:0812.2033](#)].

- [14] A. A. Klypin, S. Gottlober, and A. V. Kravtsov, *Galaxies in N-body Simulations: overcoming the overmerging problem*, *Astrophys. J.* **516** (1999) 530–551, [[astro-ph/9708191](#)].
- [15] M. Vogelsberger, A. Helmi, V. Springel, S. D. M. White, J. Wang, C. S. Frenk, A. Jenkins, A. Ludlow, and J. F. Navarro, *Phase-space structure in the local dark matter distribution and its signature in direct detection experiments*, *MNRAS* **395** (May, 2009) 797–811, [[arXiv:0812.0362](#)].
- [16] M. Kamionkowski and S. M. Koushiappas, *Galactic Substructure and Direct Detection of Dark Matter*, *Phys. Rev.* **D77** (2008) 103509, [[arXiv:0801.3269](#)].
- [17] J. Diemand, B. Moore, and J. Stadel, *Velocity and spatial biases in CDM subhalo distributions*, *Mon. Not. Roy. Astron. Soc.* **352** (2004) 535, [[astro-ph/0402160](#)].
- [18] R. Wojtak, E. L. Lokas, S. Gottloeber, and G. A. Mamon, *Radial velocity moments of dark matter haloes*, *Mon. Not. Roy. Astron. Soc.* **361** (2005) L1, [[astro-ph/0503391](#)].
- [19] S. H. Hansen, B. Moore, M. Zemp, and J. Stadel, *A universal velocity distribution of relaxed collisionless structures*, *JCAP* **0601** (2006) 014, [[astro-ph/0505420](#)].
- [20] S. H. Hansen and B. Moore, *A universal density slope Velocity anisotropy relation for relaxed structures*, *New Astronomy* **11** (Mar., 2006) 333–338, [[arXiv:astro-ph/0411473](#)].
- [21] B. Moore, C. Calcáneo-Roldán, J. Stadel, T. Quinn, G. Lake, S. Ghigna, and F. Governato, *Dark matter in Draco and the Local Group: Implications for direct detection experiments*, *Phys. Rev. D* **64** (Sept., 2001) 063508+, [[arXiv:astro-ph/0106271](#)].
- [22] C. Savage, K. Freese, and P. Gondolo, *Annual Modulation of Dark Matter in the Presence of Streams*, *Phys. Rev.* **D74** (2006) 043531, [[astro-ph/0607121](#)].
- [23] J. D. Vergados, S. H. Hansen, and O. Host, *Impact of going beyond the Maxwell distribution in direct dark matter detection rates*, *Phys. Rev. D* **77** (Jan., 2008) 023509+, [[arXiv:0711.4895](#)].
- [24] M. Fairbairn and T. Schwetz, *Spin-independent elastic WIMP scattering and the DAMA annual modulation signal*, *JCAP* **0901** (2009) 037, [[arXiv:0808.0704](#)].
- [25] J. March-Russell, C. McCabe, and M. McCullough, *Inelastic dark matter, non-standard halos and the DAMA/LIBRA results*, *Journal of High Energy Physics* **5** (May, 2009) 71+, [[arXiv:0812.1931](#)].
- [26] F. Ling, E. Nezri, E. Athanassoula, and R. Teyssier, *Dark Matter Direct Detection Signals inferred from a Cosmological N-body Simulation with Baryons*, *ArXiv e-prints* (Sept., 2009) [[arXiv:0909.2028](#)].
- [27] S. Chang, G. D. Kribs, D. Tucker-Smith, and N. Weiner, *Inelastic Dark Matter in Light of DAMA/LIBRA*, *Phys. Rev.* **D79** (2009) 043513, [[arXiv:0807.2250](#)].
- [28] W. Dehnen and J. Binney, *Local stellar kinematics from Hipparcos data*, *Mon. Not. Roy. Astron. Soc.* **298** (1998) 387–394, [[astro-ph/9710077](#)].
- [29] J. D. Lewin and P. F. Smith, *Review of mathematics, numerical factors, and corrections for dark matter experiments based on elastic nuclear recoil*, *Astropart. Phys.* **6** (1996) 87–112.
- [30] L. Hernquist, *N-body realizations of compound galaxies*, *Astrophys. J. Suppl.* **86** (1993) 389–400.

- [31] S. Kazantzidis, J. Magorrian, and B. Moore, *Generating Equilibrium Dark Matter Halos: Inadequacies of the Local Maxwellian Approximation*, *Astrophys. J.* **601** (2004) 37–46, [[astro-ph/0309517](#)].
- [32] N. Afshordi, R. Mohayaee, and E. Bertschinger, *Hierarchy in the Phase Space and Dark Matter Astronomy*, *ArXiv e-prints* (Nov., 2009) [[arXiv:0911.0414](#)].
- [33] M. Vogelsberger, S. D. M. White, A. Helmi, and V. Springel, *The fine-grained phase-space structure of cold dark matter haloes*, *MNRAS* **385** (Mar., 2008) 236–254, [[arXiv:0711.1105](#)].
- [34] M. C. Smith *et al.*, *The RAVE Survey: Constraining the Local Galactic Escape Speed*, *Mon. Not. Roy. Astron. Soc.* **379** (2007) 755–772, [[astro-ph/0611671](#)].
- [35] D. P. Snowden-Ifft, T. Ohnuki, E. S. Rykoff, and C. J. Martoff, *Neutron recoils in the DRIFT detector*, *Nuclear Instruments and Methods in Physics Research A* **498** (Feb., 2003) 155–164.
- [36] H. Nishimura, K. Miuchi, K. Hattori, S. Iwaki, C. Ida, S. Kabuki, H. Kubo, S. Kurosawa, H. Sekiya, A. Takada, M. Takahashi, A. Takeda, T. Tanimori, K. Tsuchiya, and K. Ueno, *Tracking performance of the NEWAGE-0.3a direction-sensitive dark matter detector*, *Astroparticle Physics* **31** (Apr., 2009) 185–191.
- [37] G. Sciolla and the DMTPC Collaboration, *The DMTPC project*, *Journal of Physics Conference Series* **179** (July, 2009) 012009–+, [[arXiv:0903.3895](#)].
- [38] D. P. Finkbeiner, T. Lin, and N. Weiner, *Inelastic Dark Matter and DAMA/LIBRA: An Experimentum Crucis*, [arXiv:0906.0002](#).
- [39] M. Lisanti and J. G. Wacker, *Disentangling Dark Matter Dynamics with Directional Detection*, [arXiv:0911.1997](#).
- [40] CDMS Collaboration, R. Abusaidi *et al.*, *Exclusion limits on the WIMP nucleon cross-section from the Cryogenic Dark Matter Search*, *Phys. Rev. Lett.* **84** (2000) 5699–5703, [[astro-ph/0002471](#)].
- [41] Y. Cui, D. E. Morrissey, D. Poland, and L. Randall, *Candidates for Inelastic Dark Matter*, *JHEP* **05** (2009) 076, [[arXiv:0901.0557](#)].
- [42] C. Arina, F.-S. Ling, and M. H. G. Tytgat, *The Inert Doublet Model and Inelastic Dark Matter*, [arXiv:0907.0430](#).
- [43] CDMS Collaboration, Z. Ahmed *et al.*, *Search for Weakly Interacting Massive Particles with the First Five-Tower Data from the Cryogenic Dark Matter Search at the Soudan Underground Laboratory*, *Phys. Rev. Lett.* **102** (2009) 011301, [[arXiv:0802.3530](#)].
- [44] XENON Collaboration, J. Angle *et al.*, *First Results from the XENON10 Dark Matter Experiment at the Gran Sasso National Laboratory*, *Phys. Rev. Lett.* **100** (2008) 021303, [[arXiv:0706.0039](#)].
- [45] KIMS Collaboration, H. S. Lee. *et al.*, *Limits on WIMP-nucleon cross section with CsI(Tl) crystal detectors*, *Phys. Rev. Lett.* **99** (2007) 091301, [[arXiv:0704.0423](#)].
- [46] G. J. Alner *et al.*, *First limits on WIMP nuclear recoil signals in ZEPLIN-II: A two phase xenon detector for dark matter detection*, *Astropart. Phys.* **28** (2007) 287–302, [[astro-ph/0701858](#)].
- [47] V. N. Lebedenko *et al.*, *Result from the First Science Run of the ZEPLIN-III Dark Matter Search Experiment*, [arXiv:0812.1150](#).

- [48] G. Angloher *et al.*, *Commissioning Run of the CRESST-II Dark Matter Search*, [arXiv:0809.1829](#).
- [49] K. Schmidt-Hoberg and M. W. Winkler, *Improved Constraints on Inelastic Dark Matter*, [arXiv:0907.3940](#).
- [50] R. Bernabei *et al.*, *Possible implications of the channeling effect in NaI(Tl) crystals*, *Eur. Phys. J.* **C53** (2008) 205–213, [[arXiv:0710.0288](#)].
- [51] F. Petriello and K. M. Zurek, *DAMA and WIMP dark matter*, *JHEP* **09** (2008) 047, [[arXiv:0806.3989](#)].
- [52] S. Chang, A. Pierce, and N. Weiner, *Using the Energy Spectrum at DAMA/LIBRA to Probe Light Dark Matter*, *Phys. Rev.* **D79** (2009) 115011, [[arXiv:0808.0196](#)].
- [53] C. Savage, G. Gelmini, P. Gondolo, and K. Freese, *Compatibility of DAMA/LIBRA dark matter detection with other searches*, *JCAP* **0904** (2009) 010, [[arXiv:0808.3607](#)].
- [54] D. Hooper, F. Petriello, K. M. Zurek, and M. Kamionkowski, *The New DAMA Dark-Matter Window and Energetic-Neutrino Searches*, *Phys. Rev.* **D79** (2009) 015010, [[arXiv:0808.2464](#)].
- [55] A. Manzur *et al.*, *Scintillation efficiency and ionization yield of liquid xenon for mono-energetic nuclear recoils down to 4 keV*, [arXiv:0909.1063](#).
- [56] X. Collaboration, *Constraints on inelastic dark matter from XENON10*, [arXiv:0910.3698](#).
- [57] C. Arina and N. Fornengo, *Sneutrino cold dark matter, a new analysis: Relic abundance and detection rates*, *JHEP* **11** (2007) 029, [[arXiv:0709.4477](#)].
- [58] N. Arkani-Hamed, D. P. Finkbeiner, T. R. Slatyer, and N. Weiner, *A Theory of Dark Matter*, *Phys. Rev.* **D79** (2009) 015014, [[arXiv:0810.0713](#)].
- [59] N. Arkani-Hamed and N. Weiner, *LHC Signals for a SuperUnified Theory of Dark Matter*, *JHEP* **12** (2008) 104, [[arXiv:0810.0714](#)].
- [60] M. Baumgart, C. Cheung, J. T. Ruderman, L.-T. Wang, and I. Yavin, *Non-Abelian Dark Sectors and Their Collider Signatures*, *JHEP* **04** (2009) 014, [[arXiv:0901.0283](#)].
- [61] C. Cheung, J. T. Ruderman, L.-T. Wang, and I. Yavin, *Kinetic Mixing as the Origin of Light Dark Scales*, [arXiv:0902.3246](#).
- [62] A. Katz and R. Sundrum, *Breaking the Dark Force*, *JHEP* **06** (2009) 003, [[arXiv:0902.3271](#)].
- [63] D. S. M. Alves, S. R. Behbahani, P. Schuster, and J. G. Wacker, *Composite Inelastic Dark Matter*, [arXiv:0903.3945](#).
- [64] M. Lisanti and J. G. Wacker, *Parity Violation in Composite Inelastic Dark Matter Models*, [arXiv:0911.4483](#).
- [65] R. Bernabei *et al.*, *New limits on WIMP search with large-mass low- radioactivity NaI(Tl) set-up at Gran Sasso*, *Phys. Lett.* **B389** (1996) 757–766.
- [66] K. Fushimi *et al.*, *Application of a large volume NaI scintillator to search for dark matter*, *Phys. Rev.* **C47** (1993) 425–428.
- [67] G. Gerbier *et al.*, *Pulse shape discrimination and dark matter search with NaI(Tl) scintillator*, *Astropart. Phys.* **11** (1999) 287–302.

- [68] D. R. Tovey *et al.*, *Measurement of scintillation efficiencies and pulse-shapes for nuclear recoils in NaI(Tl) and CaF-2(Eu) at low energies for dark matter experiments*, *Phys. Lett.* **B433** (1998) 150–155.
- [69] S. Yellin, *Finding an upper limit in the presence of unknown background*, *Phys. Rev.* **D66** (2002) 032005, [[physics/0203002](#)].
- [70] DAMA Collaboration, R. Bernabei *et al.*, *The DAMA/LIBRA apparatus*, [arXiv:0804.2738](#).
- [71] P. Sorensen *et al.*, *The scintillation and ionization yield of liquid xenon for nuclear recoils*, *Nucl. Instrum. Meth.* **A601** (2009) 339–346, [[arXiv:0807.0459](#)].
- [72] D. B. Cline, W. Ooi, and H. Wang, *Constraints on Inelastic Dark Matter Signal using ZEPLIN- II Results*, [arXiv:0906.4119](#).
- [73] CRESST Collaboration, F. Probst, , [Talk given at the 12th Marcel Grossman Meeting, July 12-18, 2009, Paris, France](#).
- [74] A. Bottino, F. Donato, N. Fornengo, and S. Scopel, *Interpreting the recent results on direct search for dark matter particles in terms of relic neutralino*, *Phys. Rev.* **D78** (2008) 083520, [[arXiv:0806.4099](#)].
- [75] A. Bottino, F. Donato, N. Fornengo, and S. Scopel, *Zooming in on light relic neutralinos by direct detection and measurements of galactic antimatter*, *Phys. Rev.* **D77** (2008) 015002, [[arXiv:0710.0553](#)].
- [76] R. Bernabei *et al.*, *Dark matter particles in the galactic halo: Results and implications from DAMA/NaI*, *Int. J. Mod. Phys.* **D13** (2004) 2127–2160, [[astro-ph/0501412](#)].